

# Effects of Hardening by Annealing and Softening by Additional Plastic Deformation in Ultrafine-Grained Al and Al-Based Alloys: Brief Review

T.S. Orlova<sup>1,2</sup>, M.Yu. Gutkin<sup>2,3,\*</sup>

<sup>1</sup> Ioffe Institute, Russian Academy of Sciences, Polytekhnicheskaya 26, St. Petersburg 194021, Russia

<sup>2</sup> Institute of Advanced Data Transfer Systems, ITMO University, Kronverksky pr. 49, St. Petersburg 197101, Russia

<sup>3</sup> Institute of Problems of Mechanical Engineering, Russian Academy of Sciences, Bolshoj 61, Vasil. Ostrov, St. Petersburg 199178, Russia

---

## Article history

Received June 04, 2023  
Accepted June 20, 2023  
Available online June 30, 2023

## Abstract

This is a brief review of recent experimental and theoretical results on the influence of low temperature annealing and subsequent small plastic deformation on microstructure, strength and ductility of ultrafine-grained Al and Al-based alloys structured by high pressure torsion. Some earlier results on this problem for ultrafine-grained Al and Al-based alloys structured by different methods of severe plastic deformation are also shortly presented. The reasons for the effects of hardening by annealing and softening by additional small plastic deformation of the materials are suggested and discussed in detail. Moreover, the influence of the temperature of mechanical testing and the alloying elements are in the focus of the review. It is shown that in the physical origin of these effects are the transformations of the defect structure of grain boundaries in the process of low temperature annealing and subsequent small plastic deformation of the ultrafine-grained Al and Al-based alloys structured by high pressure torsion.

---

*Keywords:* Ultrafine-grained materials; Al; Al-based alloys; Non-equilibrium grain boundaries; Dislocations

## 1. INTRODUCTION

Ultrafine-grained (UFG) aluminum-based alloys have been the subject of intense investigations, because they often exhibit unique mechanical and functional properties, such as high strength, reduced or even no strain hardening, high strain rate sensitivity, etc. [1–6] and promising for wide range of applications [1]. These unique mechanical properties of UFG metals are explained by the underlying deformation mechanisms in which grain boundaries (GBs) play the key role [5–11].

Recently, two new phenomena have been reported for commercially pure (CP) aluminum (Al) with UFG structure. It was shown that annealing can cause hardening, and the subsequent small severe plastic deformation (SPD) can lead to softening in UFG Al and some UFG Al-based alloys structured by SPD [12–31]. These phenomena are called annealing-induced hardening (AIH) and deformation-induced softening (DIS), respectively. Such behavior is atypical for

ordinary coarse-grained (CG) metallic materials, in which plastic deformation usually yields hardening, whereas post deformation annealing results in softening. Recent reviews [32,33] are devoted to manifestation of the AIH and DIS phenomena in different metals.

Meanwhile, however, significant advances which have been achieved in this field in the last few years are omitted in these reviews. In particular, a drastic effect of AIH and associated effect of DIS have been revealed recently in CP Al processed by high-pressure torsion (HPT). Both the effects in the HPT-processed Al have been elucidated experimentally and by means of theoretical modeling, including the influence of low alloying with some elements (Zr, Cu), tensile test temperature, and strain rate. The present review is an attempt to incorporate these new results into the existing knowledge on the AIH and DIS effects in Al and Al-based alloys structured by SPD.

In this review, we try to summarize briefly the existing knowledge in the field of AIH and DIS effects in Al

---

\* Corresponding author: M.Yu. Gutkin, e-mail: [m.y.gutkin@gmail.com](mailto:m.y.gutkin@gmail.com)

and low-doped Al-based alloys with UFG structure processed by severe plastic deformation methods such as equal-channel angular pressing (ECAP), HPT, accumulative roll bonding (ARB), and others. Special attention is paid to recent experimental and theoretical findings for Al and Al-based alloys with UFG structure formed by HPT processing.

First, the AIH and DIS effects are discussed for UFG pure or nearly pure Al, then the influence of low doping is considered. The impact of deformation temperature and strain rate on these effects is also briefly presented. It is necessary to note that only those hardening and softening phenomena are considered as AIH and DIS effects, respectively, that are not caused by precipitation hardening and/or change of the grain size. The experimentally obtained results and developed theoretical models are discussed in separate Sections 2 and 3.

## 2. EXPERIMENTAL FINDINGS

### 2.1. AIH and DIS effects in UFG Al

Huang et al. [12] observed that UFG Al (99.2%) processed by ARB can be hardened by annealing (the AIH effect) at low temperature and softened when subsequently deformed (the DIS effect), which is in contrast to the typical behavior of ordinary CG metals. It was reported that annealing of the ARB-processed Al at 150 °C for 0.5 h led to ~9% increase of the yield stress (curve 2, Fig. 1) and the total elongation decreased markedly, making the material almost brittle. When subsequent cold rolling with 15% of rolling reduction was applied to the annealed UFG samples, the yield stress reduced and the elongation increased so that the stress-strain curve became similar to that before the low temperature annealing (Fig. 1b).

The AIH and DIS effects first reported by Huang et al. [12] were totally new phenomena not observed in CG metals. To prove that these phenomena were not caused by any dissolution and reprecipitation of impurities, if they occurred, similar experiments were carried out using 99.99% pure aluminum as the starting material [12,13]. It was found that both effects occur in pure Al, too. Following the authors [12,14], the AIH and DIS phenomena in ARB-processed Al were related to a decrease in the density of mobile lattice dislocations (LDs) after annealing and to its increase after subsequent additional strain, respectively. They argued that the high-angle GBs (HAGBs) can act as efficient dislocation sinks, hence annealing should lead to a continuous decrease in the defect density within the grains [12,14]. Therefore, a much higher stress compared to that in the state without annealing is required to initiate plastic deformation after the annealing, as some pre-existing intragranular mobile LDs annihilated and the number of dislocation sources in grain interiors decreases, while the additional ARB deformation after annealing restores the dislocation density in grain interiors [12,14].

A somewhat higher AIH effect (~14% increase in yield strength) was found for ARB treated CP Al when electric pulse annealing (ESP) was used instead of conventional air furnace annealing, with the hardening kinetics being substantially faster for the ESP material [15].

Later Miyajima et al. [16], using scanning transmission electron microscopy (STEM) observations in combination with precise measurements of electrical resistivity, studied the evolution of microstructure under annealing and obtained a comparable change in the density of interior dislocations from an initial value of  $1.3 \cdot 10^{14} \text{ m}^{-2}$  down to  $4 \cdot 10^{13} \text{ m}^{-2}$  for ARB-processed CP Al (99.1%) after a similar low temperature annealing. The authors [16] concluded that the change in dislocation

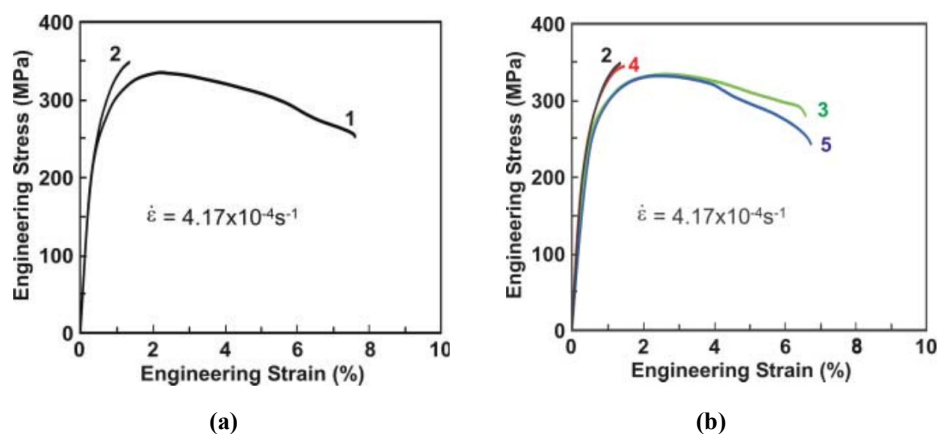


**Fig. 1.** (a) Engineering stress-strain curves for 99.2% pure Al. Curve 1: processed by six ARB cycles to an equivalent strain of 4.8. Curve 2: same as 1, plus annealing at 150 °C for 0.5 h. The strain rate used for the tensile test is indicated. (b) Engineering stress-strain curves for 99.2% pure Al. Curve 2: ARB annealed at 150 °C for 0.5 h (the same as curve 2 in Fig. 1a). Curve 3: same as 2 but deformed 15% by cold rolling. Curve 4: same as 3 but again annealed at 150 °C for 0.5 h. Curve 5: same as 4, but deformed 15% by cold rolling. Adapted from Ref. [12].

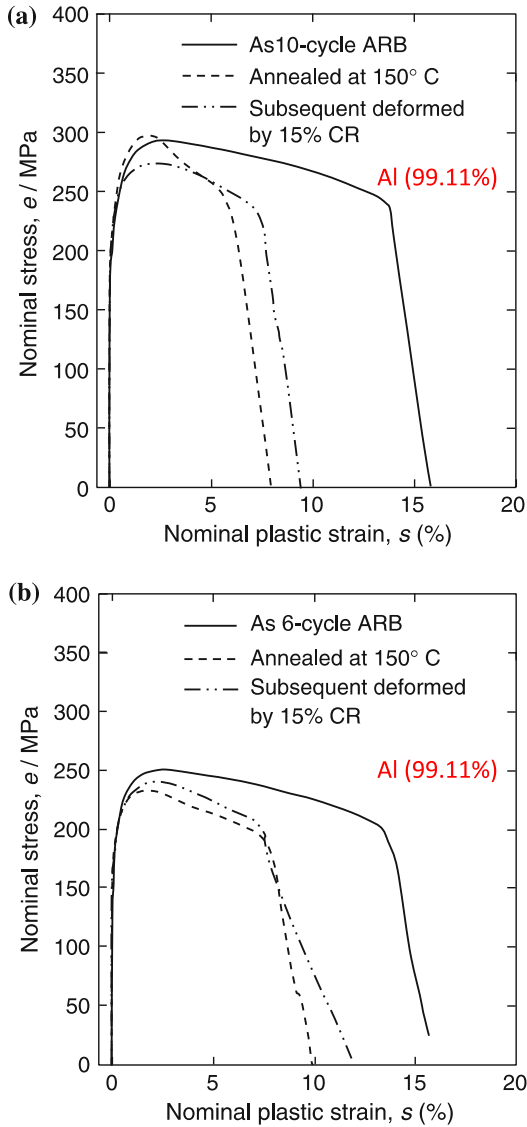


**Fig. 2.** The nominal stress-strain curves of the (a) 10-cycle ARB-processed specimens and (b) 6-cycle ARB-processed specimens. The curves for the specimens annealed at 150 °C for 1.8 ks after the ARB and for the specimens subsequently deformed by 15% cold rolling after the 150 °C annealing were also shown in the figures. Adapted from Ref. [17].

density was not dramatically high to explain the origin of the abnormal mechanical properties of UFG metals. They supposed that the AIH and DIS effects are probably somehow related to the thermally activated depinning of dislocations emitted from GBs, as is the case in the theory proposed by Kato [34].

Studying the UFG aluminum fabricated by various cycles of the ARB process, the authors of [17] reported that the specimen ARB-processed by ten cycles certainly showed the AIH and DIS effects (Fig. 2a). On the other hand, the 6-cycle specimen did not show the phenomena but was normally softened by annealing and hardened by deformation (Fig. 2b). The dislocation density in the annealed 6-

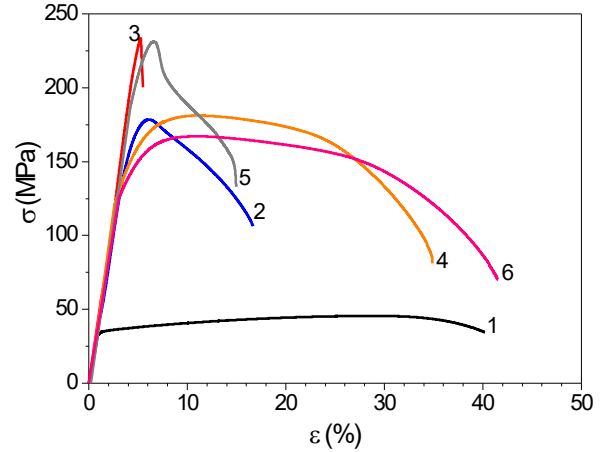


**Fig. 3.** Stress-strain diagram of CP Al specimens: (1) initial CG state, (2) after 10-revolution HPT at room temperature, (3) after HPT and annealing at 150 °C, 1 h; (4) after the treatment similar to the treatment for (3) plus 0.25-revolution HPT at room temperature; (5) the same treatment as that for (4) plus annealing at 150 °C for 1 h; (6) the same treatment as that for (5) plus 0.25-revolution HPT at room temperature. Adapted from Ref. [19].

cycle specimen was higher than that in the annealed 10-cycle specimen. The lower dislocation density was suggested to result in the occurrence of the phenomena in the latter case.

It should be noted that hardening by annealing was not also observed in a number of UFG structures of CP Al. For example, for CP Al (99.5 wt.%) in which the UFG structure was obtained by rotary swaging [35] or ECAP [36,37], the subsequent annealing at temperatures up to 175 °C did not lead to any change in microhardness. Such difference in manifestation of the AIH effect in UFG Al, structured by different SPD methods is most likely due to specific features of the UFG structures obtained by various methods and regimes of SPD.

Colossal AIH effect has been recently revealed in HPT-processed Al (99.5 wt.%) (Fig. 3) [18,19]. Extremely high increases in the conventional yield stress (YS) up to 50% and ultimate tensile strength (UTS) up to 30% were obtained by annealing of this UFG material in the range 90–200 °C for 1 h, however, the ductility of the specimen decreased significantly (Fig. 4). The maximum increase (the peak-effect) in the strength was attained after annealing at  $T_{an} = 150$  °C (Fig. 4a), during which the ductility decreased to the minimum value  $\delta \approx 1\%$  (Fig. 4b). Subsequent deformation by HPT to 0.25 turns resulted in drastic increase of plasticity to  $\sim 32\%$ , while strength slightly decreased, but retained the values typical for the HPT state (Fig. 3, curve 4). Implementation of high ductility ( $\sim 40\%$ ) at the level of CG Al, while maintaining high strength of the HPT-processed sample was demonstrated and achieved by repeating the low temperature annealing followed by subsequent additional HPT deformation (Fig. 3, curve 6) [18,19].

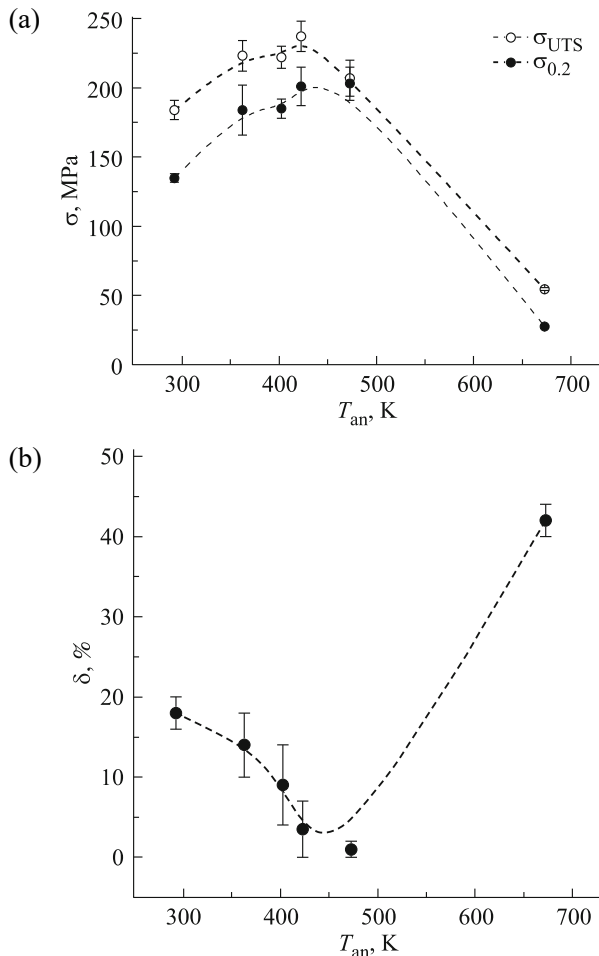


**Fig. 4.** (a) Yield stress  $\sigma_{0.2}$  and ultimate tensile strength  $\sigma_{UTS}$  of HPT-processed Al versus the annealing temperature. (b) Elongation-to-failure  $\delta$  of HPT-processed Al versus the annealing temperature. Adapted from Ref. [18].

Even higher AIH effect (88% increase of YS) was observed in Al (99.7 wt.%) processed by HPT in the same conditions [20]. Such increases were also accompanied by a sharp drop in ductility down to 1%.

As was shown experimentally [18–20], the annealing and subsequent additional deformation by 0.25–0.75 turns led to decrease and increase of dislocation density, respectively, by several times in HPT-processed Al, while the other main microstructural parameters (grain size, distribution of GBs on misorientation angles) were nearly unchanged. Since the grain interiors were nearly free of dislocations in all the studied states (before and after the annealing and after the annealing and additional HPT deformation), it was concluded that the dislocation density changes occur in GBs and nearby GB areas [19,20]. Moreover, in recent experiments, two different types of additional deformation by HPT and by cold rolling (CR) were applied after annealing of the HPT processed Al [20]. Both the types of additional deformation (0.25 HPT and 3% CR) after annealing at 150 °C for 1 h resulted in

comparable increases of dislocation density determined by X-ray diffraction (XRD) analysis. However, the additional HPT deformation to 0.25 turns after annealing led to the manifestation of a drastic DIS effect (increase of elongation to failure  $\delta$  from 1 to 23% accompanied by some decrease of UTS and YS) in the UFG CP Al structured by HPT. The change of the type of additional deformation from HPT to CR did not cause any DIS effect, but slight hardening occurred and plasticity remained at low level (1–3%). The TEM investigation showed that the key reason for such different behavior was the location of dislocations introduced into the structure of the material during additional SPD, which apparently determines either absence or manifestation of the DIS effect. In the case of 3% CR, a developed dislocation structure was observed in the grain interiors. In the case of 0.25 HPT, the grain interiors were nearly free of dislocations and additional dislocation density was concluded to be introduced in GBs and near GB areas. This points to the key role of nonequilibrium state of GBs in the manifestation of a drastic DIS effect [20].

The observations of pronounced wide extinction contours at the GBs [20,38] and separate dislocations “entering” into GBs [20] point to nonequilibrium character of GBs in the HPT-processed Al. Narrowing of extinction contours at the GBs due to short-term low-temperature annealing of HPT-processed Al was observed in [38]. Such annealing resulted in a decrease of specific electrical resistivity of GBs by  $\sim 50\%$  [38] and a decrease of average GB specific energy by  $0.3 \text{ J}\cdot\text{m}^{-2}$  [39] as was shown by differential scanning calorimetry measurements. All these findings point to relaxation of GBs during such annealing and support the conception on the decisive role of GB relaxation in the AIH effect in the HPT-processed Al.

Dependencies of the microhardness on the annealing duration at various annealing temperatures were investigated for HPT-processed CP Al in [21]. It was shown that the strength first increases linearly with the duration of annealing and then reaches saturation (Fig. 5a). The kinetic parameters of hardening by annealing (the hardening rate and the activation energy  $Q_a$ ) were determined. The obtained value  $Q_a \approx 57 \text{ kJ}\cdot\text{mol}^{-1}$  for HPT-processed CP Al was comparable with the energy of grain-boundary self-diffusion in aluminum that agrees with the conception on the decisive role of GB relaxation in the AIH effect in the HPT-processed Al.

## 2.2. Influence of low-doping on AIH and DIS effects

### 2.2.1. Al–Zr system

The effect of significant additional strengthening after low-temperature annealing was revealed in the UFG Al–

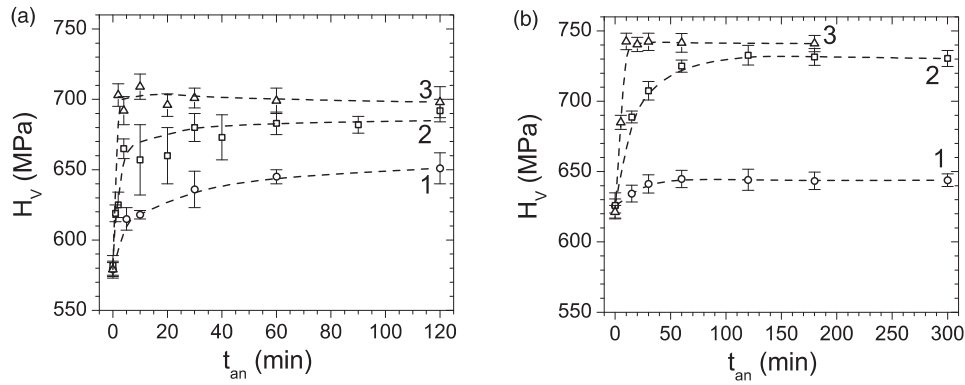


**Fig. 5.** Microhardness versus annealing time for (a) HPT-processed CP Al at annealing temperatures of 90 °C (curve 1), 130 °C (curve 2) and 150 °C (curve 3), and for (b) HPT-processed Al-Zr alloy at annealing temperatures of 90 °C (curve 1), 150 °C (curve 2) and 230 °C (curve 3). Adapted from Ref. [21].

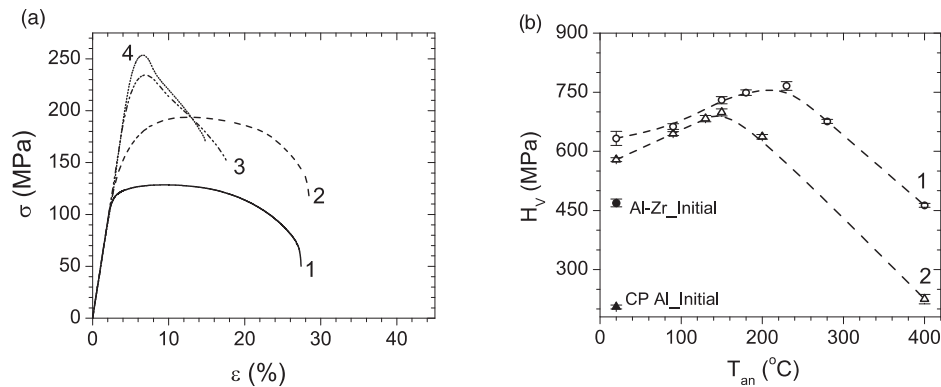


**Fig. 6.** (a) Stress-strain diagrams of Al-Zr alloy in initial state (curve 1), after HPT processing (curve 2), after subsequent annealing at 150 °C (curve 3) and at 230 °C (curve 4). (b) Microhardness ( $H_V$ ) versus annealing temperature of HPT-processed Al-Zr alloy (curve 1) and HPT-processed CP Al (curve 2). The duration of each annealing was 1 h. The values of  $H_V$  before HPT-processing are also presented. Adapted from Ref. [21].

0.4Zr (wt.%) alloy structured by HPT processing at room temperature (RT) [21,22]. A drastic hardening effect by short-term annealing in the temperature range of 90–280 °C was observed. The maximum increases in the YS (by 65%) and the UTS (by 30%) were reached as a result of annealing at 230 °C for 1 h (Fig. 6a). At the same time, the plasticity of the UFG alloy remained at a sufficiently high level of ~12%. It should be noted that approximately similar AIH effects were observed in the HPT-processed Al–0.4Zr (wt.%) which was pre-aged for formation of dispersive nanoprecipitates of  $Al_3Zr$  [22] and without such pre-aging [21]. It was shown that doping of Al by 0.4 wt.% Zr did not cause a significant impact on the magnitude of AIH effect in the annealing temperature range 90–150 °C, however, it led to its further increase, shifting its maximum to  $T_{an} \sim 230$  °C and expanding the range of its existence up to  $T_{an} = 280$  °C (Fig. 6b). The study of the kinetics of hardening by annealing in the HPT-processed Al-Zr alloy showed that microhardness first increases linearly with the duration of annealing and then reaches saturation like in the HPT Al (Fig. 5b) [21]. The addition of Zr was found to result

in the reduction of the activation energy of AIH by ~2 times compared with  $Q_a$  value in HPT Al.

Microstructural studies of the HPT-processed Al-Zr (0.4 wt.%) alloy showed that the grain size, the fraction of HAGBs and the average misorientation angle remain practically unchanged after annealing in the temperature range of  $T_{an} = 90$ –230 °C [21,22]. According to TEM data, such deformation-heat treatment (DHT, i.e. the annealing and the small HPT deformation) did not noticeably change the size and distribution of disperse precipitates of  $Al_3Zr$  secondary phase, which were observed in small amount by TEM [21,22]. The only parameter which was substantially changed by such annealing, was the dislocation density determined by XRD. As was supposed in Refs. [21,22], the relaxation of HAGBs through decrease in dislocation density and possible formation of segregation/nanoprecipitates in them are the most probable reasons for the AIH effect in the Al-Zr alloy.

In-situ annealing at 230 °C for 3 h in a scanning transmission electron microscope revealed no noticeable displacement of GBs, but slight rearrangement of GB orientations such as straightening and approaching the angles

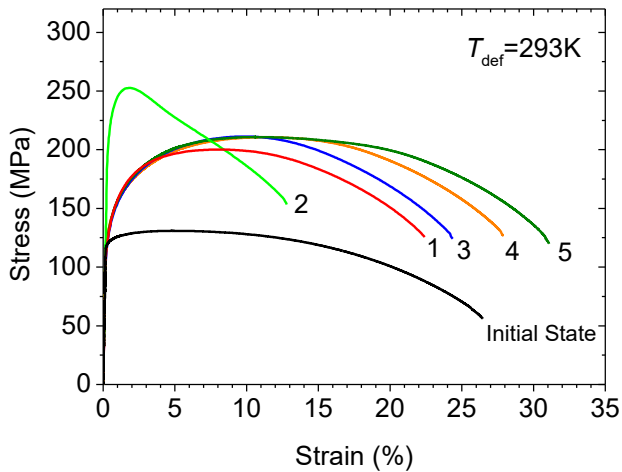


**Fig. 7.** The stress-strain curves for the Al-0.4Zr alloy in the initial state, after HPT-processing (curve 1), after HPT-processing and subsequent annealing at 230 °C for 1 h (curve 2), after annealing and additional HPT deformation to 0.25 (curve 3), 0.5 (curve 4) and 0.75 (curve 5) turns. Adapted from Ref. [24].

between them to 120° [23]. Such observations were related to relaxation of GBs during the annealing.

The DIS effect accompanied by a significant increase in ductility was reported in Ref. [24] for the UFG Al-0.4Zr (wt.%) alloy structured by HPT. Additional HPT to 0.25 turns led to a decrease in the UTS and YS values, while the magnitudes of elongation to failure and the uniform elongation substantially increased to the values typical for the HPT state (Fig. 7). An increase in the value of additional deformation from 0.25 to 0.75 turns led to a further increase in ductility to 30%, which exceeded the ductility of the alloy in the initial state before HPT treatment while maintaining its high strength of the HPT state (Fig. 7).

### 2.2.2. Al-Cu and Al-Cu-Zr systems

The influence of Cu doping on the AIH and DIS effect were studied in Al-1.5Cu (wt.%) [25] and Al-1.47Cu-0.34Zr (wt.%) [26,27] alloys. Short-term annealing at different  $T_{an}$  from the range 100–200 °C for different duration from few min to 1 h showed that the microhardness first decreases with increasing annealing time and then reaches a saturation level in both alloys. Tensile tests also showed a decrease of YS after such annealing, but elongation to failure dropped to ~1% (Fig. 8a) in the Al-1.5Cu (wt.%) and to ~3% in the Al-Cu-Zr alloy (Fig. 8b). Thus, the AIH effect does not manifest itself in these systems, but plasticity drops to a very low level. However, the subsequent small HPT deformation to 0.25 turns caused drastic increase in plasticity (the DIS effect) (Fig. 8) in both systems. In the Al-Cu-Zr system, such DHT consisting of annealing and additional deformation, caused the ductility increase from ~3–5 to 11% (the DIS effect) at RT while maintaining a high strength of ~465 MPa (Fig. 8b).

Detailed microstructural studies were performed for the Al-Cu-Zr alloy in Refs. [26,27]. It was shown that the HPT processing resulted in formation of UFG structure with the average grain size of ~285 nm. Such specific features as formation of the  $\theta$  phase ( $Al_2Cu$ ) with sizes of ~20–40 nm was observed at GBs (Fig. 9). The grain size in the UFG structure formed by HPT processing did not practically change after annealing and after annealing and additional 0.25 HPT deformation. After annealing the precipitates increased in size (~60 nm), their shape becomes less rounded, but more angular, and did not change visually after subsequent additional deformation. The dislocation density  $L_{dis}$  decreased after annealing by 1.5 times and increased after subsequent 0.25 HPT deformation by 1.8

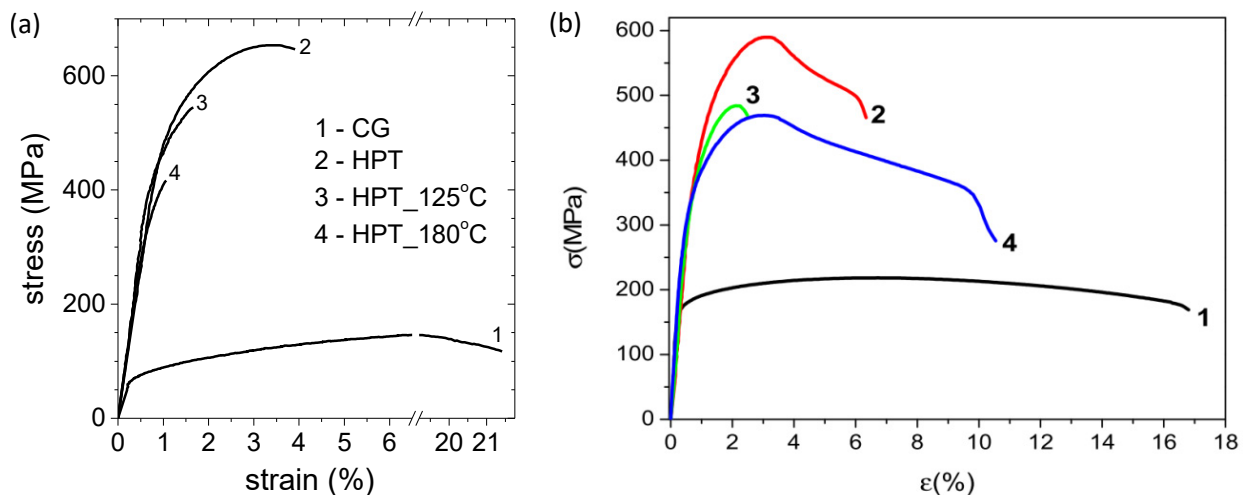


**Fig. 8.** (a) Stress-strain curves of Al-1.5Cu (wt.%) alloy in the initial coarse-grained state (curve 1), after HPT processing (curve 2), after annealing at 125 °C, 1 h (curve 3), after annealing at 180 °C, 1 h (curve 4). Adapted from Ref. [25]. (b) Stress-strain curves of Al-1.47Cu-0.34Zr (wt.%) alloy in the initial pre-aged state (AG state) (curve 1), after HPT processing (curve 2), after annealing at 125 °C, 4 h (curve 3), after the annealing and additional 0.25 HPT deformation (curve 4). Adapted from Ref. [26].

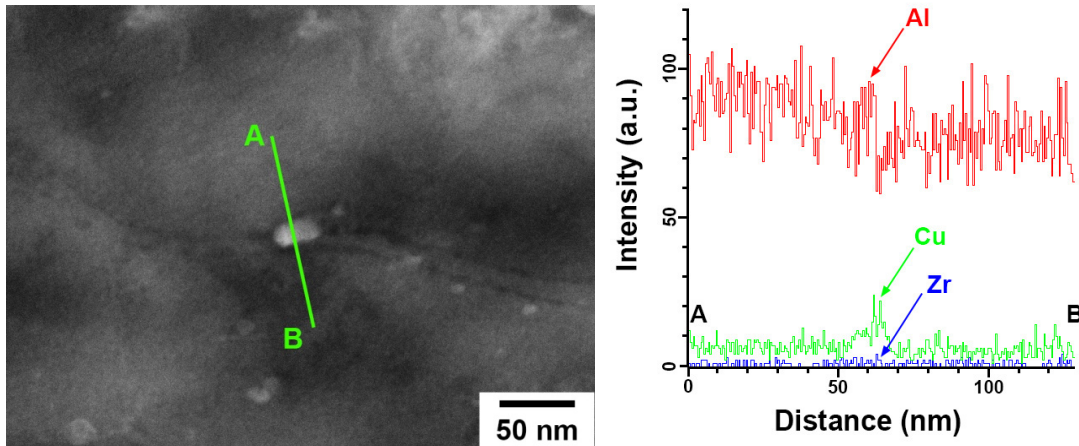


**Fig. 9.** STEM image with the EDX line scan analysis of secondary phase precipitate at a GB in the HPT-processed Al–Cu–Zr alloy. EDX is the energy dispersive X-ray analysis. Adapted from Ref. [27].

times. In the HPT state,  $L_{dis}$  was  $2.6 \cdot 10^{13} \text{ m}^{-2}$ . The absence of AIH effect and drastic DIS effect in the Al–Cu–Zr alloy were related to the change of GB structural parameters (the size and shape of  $\text{Al}_2\text{Cu}$  nanoprecipitates and the dislocation density) [26,27].

### 2.2.3. Al–Mg system

An increase of microhardness  $H_V$  with the annealing temperature was observed in HPT-processed Al–1.5Mg alloy with grain size of 150 nm long ago [40]. The increase of  $H_V$  occurred in the annealing temperature range of 347–423 K with peak-effect at 373 K. The authors explained such non-typical behavior by higher transparency of nonequilibrium GBs for mobile dislocations, referring to the fact that dislocations are easier absorbed and nucleated at those GBs that are less ordered [41,42]. According to Ref. [40], during the annealing at the homologous temperature of 0.37, the GBs relaxed and their Hall-Petch hardening effect became higher. The term “GB relaxation” means that the excess defects in the GBs are annihilated and the GB structure becomes more equilibrated. No studies of influence of subsequent additional deformation were performed that time.

Later it was shown that Mg segregated at GBs in Al–Mg alloys during their structuring by HPT processing [43–45]. Segregation of Mg in the GBs were detected by atom probe tomography and energy-dispersive X-ray spectroscopy in STEM in Al–Mg alloys (including the alloys with low Mg concentration of  $\sim 0.5 \text{ wt.}\%$  [45]) during their HPT processing even at RT. Hence annealing can change the segregation parameters and thereby change the strength. As was shown in [45,46], segregation of Mg in GBs did lead to additional hardening of UFG Al–Mg–Si and Al–Mg alloys. In addition, as was shown in Ref. [47], a similar annealing (at 423 K, 1 h) of the HPT-processed Al–1Mg (wt.%) alloy led to substantial decrease of tensile

strength (YS and UTS), that contradicts the results of [40]. Actually, systematic studies of relationship between changes in all basic microstructural parameters and mechanical properties under annealing and additional deformation of UFG Al–Mg alloys are still missed and needed to shed light on this problem.

### 2.3. Influence of temperature and strain rate of tensile testing

The influence of tensile test temperature (deformation temperature  $T_{def}$ ) on the AIH and DIS effects was investigated for UFG Al (99.6 wt.%) [28], UFG Al–0.4Zr (wt.%) [24], and UFG Al–1.47Cu–0.34Zr [27]. The UFG structures in all studied systems were formed by HPT processing at 6 GPa to 10 turns. The revealed AIH and/or DIS effects at RT in these UFG alloys are briefly described above in Section 2.2.

The temperature dependences of the YS ( $\sigma_{0.2}$ ), UTS ( $\sigma_{UTS}$ ), uniform ductility  $\delta_1$  and total ductility  $\delta$  were obtained and analyzed for three states: as-HPT-processed (HPT state), after corresponding low temperature annealing (HPT+AN state) and after such annealing and additional HPT deformation to 0.25 turns (HPT + AN + 0.25HPT state). It was found for the HPT-processed Al that annealing-induced increase of  $\sigma_{0.2}$  and  $\sigma_{UTS}$  decreases with decreasing  $T_{def}$  (Figs. 10a,b) and the AIH effect completely disappears at  $T_{def} \sim 193 \text{ K}$  and  $\sim 223 \text{ K}$  for  $\sigma_{0.2}$  and  $\sigma_{UTS}$ , respectively, whereas suppression of ductility by annealing is kept up to 193 K, at least (Fig. 10c) [28]. Similar to behavior at RT, at the decreased temperatures, small additional HPT deformation to 0.25 turns after annealing results in softening (decrease in  $\sigma_{0.2}$  and  $\sigma_{UTS}$ ) and increase in ductility (curves 3 in Fig. 10). However, the magnitude of DIS effect decreases with decrease of  $T_{def}$ , becoming negligible at  $T_{def} < 193 \text{ K}$  (Fig. 10c).

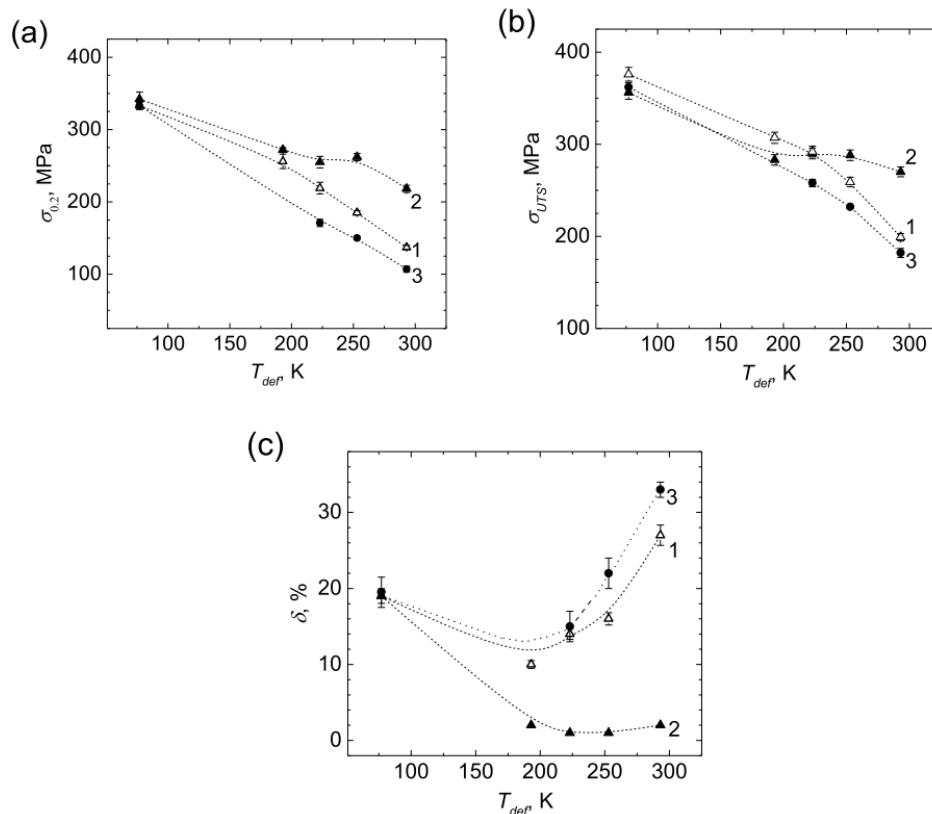


**Fig. 10.** Yield stress (a), ultimate tensile strength (b) and elongation-to-failure (c) versus deformation temperature for Al after HPT-processing (curve 1), after HPT-processing and annealing at 150 °C for 1 h (curve 2), after HPT-processing, annealing and subsequent additional HPT deformation to 0.25 turns (curve 3). Adapted from Ref. [28].

Similar to the case of HPT-processed Al, both the AIH and DIS effects weaken with a decrease in the tensile test temperature in the HPT-processed Al-0.4Zr alloy [24]. Alloying with Zr expands the temperature range of the AIH effect manifestation to lower temperatures as compared to the similar effect in CP Al. For example, the AIH effect still occurs at 193 K (the YS increase is about 46 MPa) in the Al-0.4Zr alloy, while it is totally suppressed in CP Al at similar temperature. The DIS effect completely disappears in the HPT-processed Al-Zr alloy at 193 K.

As was shown in Section 2.2, the AIH effect is absent in Al-1.47Cu-0.34Zr alloy, but the DIS effect occurs after additional 0.25 HPT deformation of the pre-annealed state. Decrease of the strength to about ~80% of the strength before DHT is accompanied by substantial increase of plasticity by nearly 4 times. Such substantial increase of plasticity was named plasticization effect (PE). The PE decreases monotonically with decreasing  $T_{def}$  and completely disappears at ~223 K (Fig. 11) [27].

Analyzing the temperature dependences of the YS, the activation energy  $Q$  of the plastic flow in the states before annealing, after annealing, and after annealing and additional deformation was estimated for HPT-processed Al [28] and for HPT-processed Al-Zr [24] and

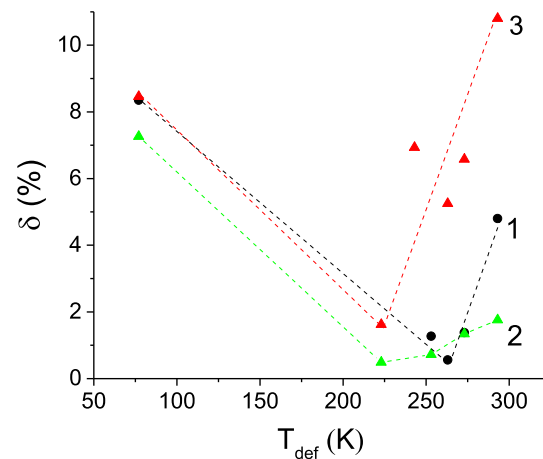


**Fig. 11.** Elongation to failure versus tensile test temperature for the Al-1.47Cu-0.34Zr (wt.%) alloy in the states: 1 – HPT, 2 – HPT+AN(125 °C, 4 h), 3 – HPT+AN(125 °C, 4 h)+0.25HPT. The strain rate is  $5 \cdot 10^{-4} \text{ s}^{-1}$ . Dashed lines are guide for eyes. Adapted from Ref. [27].

Al-Cu-Zr [27] alloys in the temperature range of manifestation of the AIH and/or DIS effects (Table 1). In the HPT state, the values of  $Q$  are comparable for Al and the both alloys. Doping by Zr (without Cu) slightly decreases the  $Q$ -value in the HPT state compared with that in Al. Annealing strongly decreases the activation energy

**Table 1.** Strain-rate sensitivity coefficient ( $m$ ) and the activation energy ( $Q$ ).

Material	State	$m$	$Q_{k=0.2\%}$ , kJ/mol
CP Al [24,28]	HPT	0.03 [48]	95±15
	HPT+AN		7.5
	HPT+AN+0.25HPT		95±17
Al-0.4Zr [24]	HPT	0.045	82±15
	HPT+AN		23±4
	HPT+AN+0.25HPT	0.045	80±17
Al-1.47Cu- 0.34Zr [27]	HPT	0.033±0.016	90±6
	HPT+AN		41±6
	HPT+AN+0.25HPT	0.038±0.011	72–82

in all these materials (Table 1). The additional deformation by 0.25 HPT restored the  $Q$ -value in Al [28] and Al-Zr [24]. In the Al-Cu-Zr alloy, in the temperature range 223–293 K, the  $Q$ -values differ in all three states, which is related to the changes in the grain boundary structure (dislocation density, size and shape of  $Al_2Cu$  nanoprecipitates) [27].

It was also shown that the PE at RT is preserved when the strain rate is changed from  $10^{-4}$  to  $10^{-3} s^{-1}$  and sharply decreases as strain rate is further increased (Fig. 12) [27]. The strain rate sensitivity coefficient ( $m$ ) was determined in the states before and after DHT, consisting of appropriate annealing and additional 0.25 HPT deformation for Al-0.4Zr [24] and Al-Cu-Zr alloys [27] (Table 1). As is seen, the DHT does not change the  $m$ -value in both alloys [24,27]. Then it was concluded in Refs. [24,27] that the PE in these alloys is not due to intensification of grain boundary sliding (GBS), because such intensification would be accompanied by an increase of  $m$ -value [48,49].

The decrease of the magnitude of AIH and DIS effects with decreasing  $T_{def}$  was explained theoretically in Refs. [24,28], see Section 3.1 for details. In particular, it was concluded [24], that the activation energy  $Q$  in the HPT state is determined by the glide of extrinsic grain-boundary dislocations (EGBDs) along GB planes, while after annealing, the EGBDs are absent or their amount is negligible, and then the  $Q$ -value is determined by the glide of LDs emitted from GBs to grain interiors [24].

### 3. THEORETICAL MODELING

#### 3.1. The case of commercially pure UFG aluminum

Soon after establishing the first experimental results on the AIH and DIS effects on UFG CP Al structured by HPT [18,19] (see also Section 2 for details), some theoretical models were suggested to describe these effects. In their elaboration, the following key ideas were used [19,51,52]:

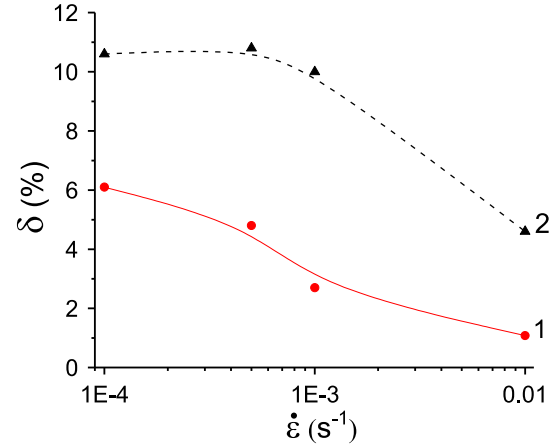


**Fig. 12.** Elongation to failure versus strain rate for the Al-1.47Cu-0.34Zr (wt.%) alloy in the states: HPT (curve 1) and HPT+AN (125 °C, 4 h) + 0.25HPT (curve 2).  $T_{def} = 293$  K. Adapted from Ref. [27].

- (i) It was accepted that, after the initial HPT treatment, the GBs have got non-equilibrium structure that is characterized by high density of extrinsic grain-boundary dislocations (EGBDs) some of which have Burgers vectors parallel to the GB planes and, therefore, can glide within the GBs.
- (ii) Under external loading, the mobile EGBDs glide along the GB planes and are stored against the GB triple junctions, thus forming dislocation pile-ups.
- (iii) When the shear stress  $\tau$  acting on the head EGBD in such a pile-up exceeds a critical value  $\tau_{c(1)}$ , the head EGBD emits a lattice dislocation (LD) that glides across the neighboring grain, reaches the opposite GB and is accepted by it.
- (iv) With further loading, some new LDs are supposed to be emitted by the pile-up if  $\tau$  reaches the corresponding critical values  $\tau_{c(n)}$ , where  $n$  is the number of the emitted LD.
- (v) When the emitted LDs reach the opposite GB and are accepted by it, they start to climb along the GB and to create a back shear stress on the new emitted dislocations. As a result, the level of  $\tau_{c(n)}$  increases, thus forming the strengthening effect. It is also assumed that the dependence of  $\tau_{c(n)}$  on the number  $n$ , which is in direct proportion with the plastic deformation, is reflected in the stress-strain curve of the sample under testing until the neck formation starts.
- (vi) Due to high initial density of EGBDs in the non-equilibrium GBs after the HPT treatment, the dislocation pile-ups in the GBs are supposed to be strong enough (in other words, they are supposed to contain many EGBDs) to emit a large number of LDs that, in their turn, can produce high back shear stress after incorporation into the structure of the opposite GB. As a result, a sample is expected to demonstrate a

combination of high strength with sufficient plasticity, as was detected in experiments (see Section 2).

- (vii) After short-time annealing that does not substantially increase the grain size but strongly changes the GB structure, transforming it to a more equilibrium state than it was before the annealing, there is no high density of EGBDs capable to glide along GBs. It is supposed that the dislocation pile-ups which may nevertheless form in the GBs, should be weak enough (in other words, they are supposed to contain few EGBDs) and need high levels of applied shear stress  $\tau$  to emit LDs by the scenarios (iii)–(v). Moreover, under such high values of  $\tau$ , the pile-ups can emit some limited numbers of LDs only and are expected to run out fast. As a result, a sample is expected to show a combination of higher strength (than before annealing) with rather low plasticity. This may explain the AIH effect observed in experiments (see Section 2).
- (viii) A small additional plastic deformation by HPT of the annealed material does not practically change the grain size but restores the non-equilibrium structure of GBs. This means that GBs again become rich with EGBDs that can glide within the GBs and form strong dislocation pile-ups which can emit many LDs by the scenarios (iii)–(v). Therefore, the annealed and additionally deformed UFG material is again expected to demonstrate high strength (although lower than in the annealed state) coupled with strongly increased plasticity, that is the DIS effect revealed in experiments (see Section 2).

Fig. 13 taken from Ref. [52] shows the sketches of the process of a defect structure transformation in HPT-processed UFG material which is tested after annealing and subsequent small HPT deformation (similar sketches are true for testing before and after annealing; the only difference between the corresponding figures is in the number  $n_{pu}$  of EGBDs in the dislocation pile-ups, see Refs. [19,51,52] for details). Fig. 13a illustrates an UFG material with two pile-ups of EGBDs that are modeled by  $\pm B$ -superdislocations (general view). Fig. 13b is the magnified inset illustrating the initial defect structure. Figs. 13c–g show the successive emission of pairs of LDs from triple junctions A and B, their capture by the GBs AE and BF, and their climb along these GBs. Fig. 13h represents the defect configuration after the  $(n-1)$ th event of the LD emission, while Fig. 13i shows the emission of the  $n$ th pair of the LDs.

According to the models [19,51,52], the total field of the external shear stress and the shear stresses of superdislocations A and B causes the emission of the first pair of LDs with Burgers vectors  $\pm \mathbf{b}$  from triple junctions A and B into adjacent grain interior (Fig. 13c). The emission of the first pair of LDs is the result of the splitting of the head

dislocations in the EGBD pile-ups into two immobile sessile dislocations with Burgers vectors  $\pm \mathbf{b}_{s1}$  and two mobile LDs with Burgers vectors  $\pm \mathbf{b}$  (hereinafter we call them  $\pm b$ -LDs) which are capable to glide in grain interior along the similar slip planes (Fig. 13c). Thus, the magnitude  $B$  of the Burgers vectors of the  $\pm B$ -superdislocations A and B decreases by the value  $b_{gb}$  and becomes equal to  $B_1 = B - b_{gb}$  (Fig. 13c).

Within the continuum approach used in the models [19,51,52], the emission of a pair of LDs in Fig. 13c corresponds to the appearance of two dipoles AC and BD of  $\pm b$ -LDs consisting of two mobile LDs (mobile  $b$ -LD C and  $-b$ -LD D), which can move inside the grain, and two immobile LDs (immobile  $-b$ -LD A and  $b$ -LD B) which remain at triple junctions A and B (Fig. 13d). The orientation of the mobile LD slip planes is determined by the angle  $\alpha$  (Fig. 13c). The distance which the first pair LDs pass within the grain, is given by the value  $p_1$  (Figs. 13c,d). To emit the first pair of the  $\pm b$ -LDs from triple junctions A and B, the external shear stress  $\tau$  must reach a certain critical value  $\tau_{c(1)}$ . After the emission, the  $\pm b$ -LDs glide in the grain until they reach the opposite GBs where they are captured by the GBs and transform into new EGBDs which can climb along GBs (Figs. 13c–e). At the same time, the sessile  $\pm \mathbf{b}_{s1}$ -dislocations react with the new head dislocations of the EGBD pile-ups forming new sessile dislocations with the Burgers vectors  $\pm \mathbf{b}_{s2}$  (Fig. 13e). This dislocation reaction reduces the magnitude  $B_1$  of the Burgers vectors of the  $\pm B$ -superdislocations and its value becomes equal to  $B_2 = B_1 - 2b_{gb}$  (Fig. 13e).

The emission of the second pair of  $\pm b$ -LDs occurs in the same way as the emission of the first pair LDs (Fig. 13f). However, the stress field of the first pair LDs hampers the emission of the second one due to the repulsive forces between them. In this case, the first pair of the  $\pm b$ -LDs creates stress fields which hamper the emission of the second pair of the  $\pm b$ -LDs. Thus, the emission of the second pair of the  $\pm b$ -LDs requires another increase in the external shear stress  $\tau$  up to a new critical value  $\tau_{c(2)} > \tau_{c(1)}$  and the second pair of the LDs cannot come closely to the LDs of the first pair occupying certain equilibrium positions  $p_2$  (Fig. 13f) within the grain. After emission of the second pair of the LDs, new sessile dislocations with Burgers vectors  $\pm \mathbf{b}_{s3} = \pm 2\mathbf{b}_{s2}$  (Fig. 13g) are formed due to the dislocation reaction between the new  $\pm \mathbf{b}_{s1}$ -dislocations (which are formed in a similar way as the first sessile  $\pm \mathbf{b}_{s1}$ -dislocations), the head  $\pm \mathbf{b}_{gb}$ -dislocations of the EGBD pile-ups and the sessile  $\pm \mathbf{b}_{s2}$ -dislocations.

The process of the emission of a new pair of LDs from triple junctions A and B can be repeated many times. Each new emission of LDs requires an increase in the external shear stress  $\tau$  to a new critical value

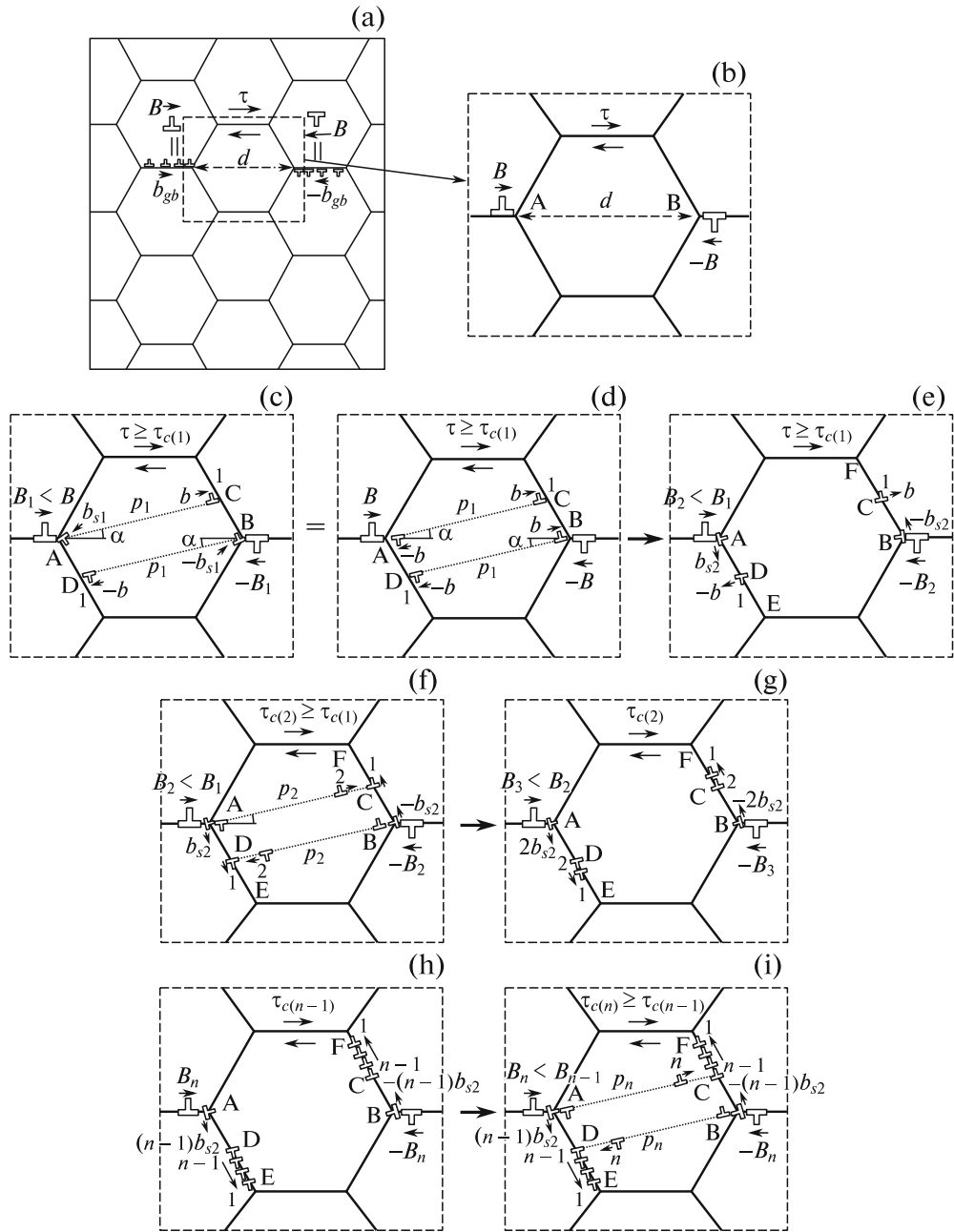


**Fig. 13.** Model of a micromechanism of the process of a defect structure transformation in HPT-processed UFG material after annealing and subsequent small HPT deformation (schematically). (a) UFG material with two pile-ups of GBDs that are modeled by  $\pm B$ -superdislocations (general view). (b) Magnified inset illustrating the initial defect structure. (c–g) Successive emission of pairs of LDs from triple junctions A and B, their capture by the GBs AE and BF, and their climb along these GBs. (h) Defect configuration after the  $(n-1)$ th event of the LD emission. (i) Emission of the  $n$ th pair of the LDs. Adapted from Ref. [52].

$\tau_{c(n)} > \tau_{c(n-1)}$  (Fig. 13i). As a result of the successive emission of the LDs and the capture of the previously emitted LDs by GBs AE and BF, two walls CF and DE of climbing EGBDs are formed (Fig. 13i).

Within the models [19,51,52], each emission of the LDs led to a decrease in the magnitude  $B_n < B_{n-1}$  of Burgers vectors of the  $\pm B$ -superdislocations (which model the pile-ups of EGBDs), thus causing a significant increase in the critical stress  $\tau_{c(n)} > \tau_{c(n-1)}$  and, as a result, a significant hardening of the UFG material subjected to annealing only. However,

the magnitude of Burgers vector of the  $\pm B$ -superdislocations in UFG materials subjected to annealing and some subsequent HPT deformation is much higher than in the UFG materials subjected to annealing only. Thus, a smoother increase in critical stress  $\tau_{c(n)}$  was expected with the emission of the LDs and a combination of deformation strengthening with rather high ductility in UFG materials subjected to annealing and additional HPT deformation.

The mathematical analysis of the model under discussion was based on the energetic approach when the authors

of [19,51,52] calculated the changes in the total energy of the defect structure after and before the  $n$ -th emission event. In the case of a decrease in the total energy, a transformation of the defect system is energetically favorable, otherwise this transformation is energetically unfavorable. Thus, on every key step of the structure transformation, the authors of [19,51,52] analyzed the energy differences numerically with determining the critical conditions for these transformations. A similar approach was used before in analyzing various models of defect structure transformations [53–62].

The LD emission process (Fig. 13) was specified by the energy difference  $\Delta W_n = W_n - W_{n-1}$ , where  $W_{n-1}$  is the energy of the  $(n-1)$ -th state of the system containing the  $n-1$  pairs of the LD dipoles (Fig. 13h), and  $W_n$  is the energy of the system after the emission of the  $n$ -th pair of LDs (Fig. 13i). Such a transformation of the defect system is energetically favorable if  $\Delta W_n = W_n - W_{n-1} < 0$ .

The energy difference  $\Delta W$  was written as [52]:

$$\Delta W_n = E_{(n)}^{2b} + E_{(n)}^{B-2b} + E_{(n)}^{2b-2b} + E_{(n)}^{2b-b} + E_{(n)}^{bs-2b} + E_{\tau(n)}, \quad (1)$$

where  $E_{(n)}^{2b}$  denotes the sum self energy of  $\pm b$ -LD dipoles AC and BD;  $E_{(n)}^{B-2b}$  is the energy of elastic interaction between the dipole of  $\pm B$ -superdislocations AB and  $\pm b$ -LD dipoles AC and BD;  $E_{(n)}^{2b-2b}$  is the energy of elastic interaction between the  $\pm b$ -LD dipoles AC and BD;  $E_{(n)}^{2b-b}$  is the energy of elastic interaction of  $\pm b$ -LD dipoles AC and BD with walls CF and DE of climbing  $\pm b$ -LDs;  $E_{(n)}^{bs-2b}$  is the energy of elastic interaction of  $\pm b$ -LD dipoles AC and BD with the sessile  $\pm(n-1)b_{s2}$ -dislocations; and  $E_{\tau(n)}$  is the interaction energy of the applied shear stress  $\tau$  with dipoles AC and BD of  $\pm b$ -LDs and walls CF and DE of climbing  $\pm b$ -LDs. All these terms were given in [51,52] in a closed analytical form that makes them rather convenient for further numerical calculations.

Using the numerically calculated dependences  $\Delta W_n(p_n)$ , where  $p_n$  were the positions of the  $n$ -th mobile LDs (see Fig. 13i), the authors [19,51,52] calculated the critical shear stress  $\tau_{c(n)}$  that is the minimum stress at which the emission of the  $n$ -th pair of LDs is energetically favorable. More precisely, the critical shear stress  $\tau_{c(n)}$  was found from the conditions that  $\Delta W_n(p_n = p') = 0$

(where  $p' = 1$  nm),  $\Delta W_n|_{p_n > p'} < 0$  and  $\frac{\partial \Delta W_n}{\partial p_n} \Big|_{p_n > p'} \leq 0$ . The

critical stress  $\tau_{c(n)}$  was related to the flow stress  $\sigma$  as follows  $\sigma = 2\tau_{c(n)} / \cos 2\alpha$ . If the inequalities  $\Delta W_n|_{p_n > p'} < 0$

and  $\frac{\partial \Delta W_n}{\partial p_n} \Big|_{p_n > p'} < 0$  were valid, the dependences of the en-

ergy change  $\Delta W_n(p_n)$  on the distance  $p_n$  moved by the LDs within a grain were monotonously decreasing and negatively valued functions. In this case, it was treated

that the emitted  $\pm b$ -LDs moved across the grain over the distance  $p_n = d / \cos \alpha$  towards the opposite GBs where they stopped. In the other case, when  $\Delta W_n|_{p_n > p'} < 0$ ,

$\frac{\partial \Delta W_n}{\partial p_n} \Big|_{p_n = p_{eq}} = 0$  and  $\frac{\partial^2 \Delta W_n}{\partial p_n^2} \Big|_{p_n = p_{eq}} > 0$ , the function

$\Delta W_n(p_n)$  had its minimum corresponding to the equilibrium distance  $p_n = p_{eq}$  moved by  $\pm b$ -LDs or, in other words, the equilibrium position  $p_{eq}$  of the  $\pm b$ -LDs in the grain interior.

With using the aforementioned approach, the authors of Refs. [19,51,52] calculated the dependence of the flow stress  $\sigma$  on the value of plastic shear deformation  $\gamma_n$  in the exemplary case of UFG Al subjected to annealing and additional HPT deformation. The value of the plastic shear deformation was estimated by the following expression  $\gamma_n \approx 2nb/d$ . The following typical values of material parameters were used [41,63]: the shear modulus  $G = 27$  GPa, the Poisson ratio  $\nu = 0.34$ , the lattice parameter  $a = 0.405$  nm,  $b = a\sqrt{2}/2$ , and  $b_{gb} \approx 0.1$  nm [64]. The grain size  $d$  and angle  $\alpha$  were taken as  $d = 1000$  nm and  $\alpha = 20^\circ$ .

Figure 14 shows the calculated in Ref. [51] dependences  $\sigma(\gamma_n)$  (solid curves) for the case of UFG aluminum after annealing with different amounts of EGBDs in pile-ups:  $n_{pu} = 120$  (curve 1), 172 (2), and 250 (3). For comparison, the experimental curves from Ref. [19] (dashed lines) for the initial coarse-grained technically pure Al (Al<sub>CG</sub>), UFG state obtained by the HPT before annealing (Al<sub>HPT</sub>) and after annealing at 150 °C for 1 h (Al<sub>HPT\_150 °C</sub>), are shown. As is seen from the experimental curves Al<sub>HPT\_150 °C</sub>, the maximum flow stress  $\sigma_y^{\text{exp}} \approx 240$  MPa is reached upon plastic deformation  $\varepsilon^{\text{exp}} \approx 5\%$  (Fig. 14).

Within the theoretical model [51], there were no restrictions on the increase in the flow stress  $\sigma$  with increasing plastic strain  $\gamma_n$ , caused by the emission and slip of LDs. Therefore, the authors considered two cases of constructing theoretical dependences  $\sigma(\gamma_n)$ . In the first case, they limited the increase in the flow stress  $\sigma$  by  $\sigma = \sigma_y^{\text{exp}}$  (Fig. 14a), at which different limiting values of the plastic strain at the stage of hardening for different values of  $n_{pu}$  were obtained. In the second case, they imposed restrictions on the growth of plastic strain  $\gamma_n$  by the value of  $\gamma_n = \varepsilon^{\text{exp}}$  (Fig. 14b) at which they got different limiting values for the flow stress for different values of  $n_{pu}$ . As a result, it was shown that a decrease in the number of EGBDs in pile-ups leads to a decrease in the plastic strain  $\gamma_n$  (Fig. 14a) and an increase in the flow stress  $\sigma$  in UFG Al (Fig. 14b). In other words, a decrease, as a result of annealing, in the number of EGBDs that make up the initial pile-ups leads to an increase in strength and a decrease in plasticity of UFG Al. At the same time, an increase in the

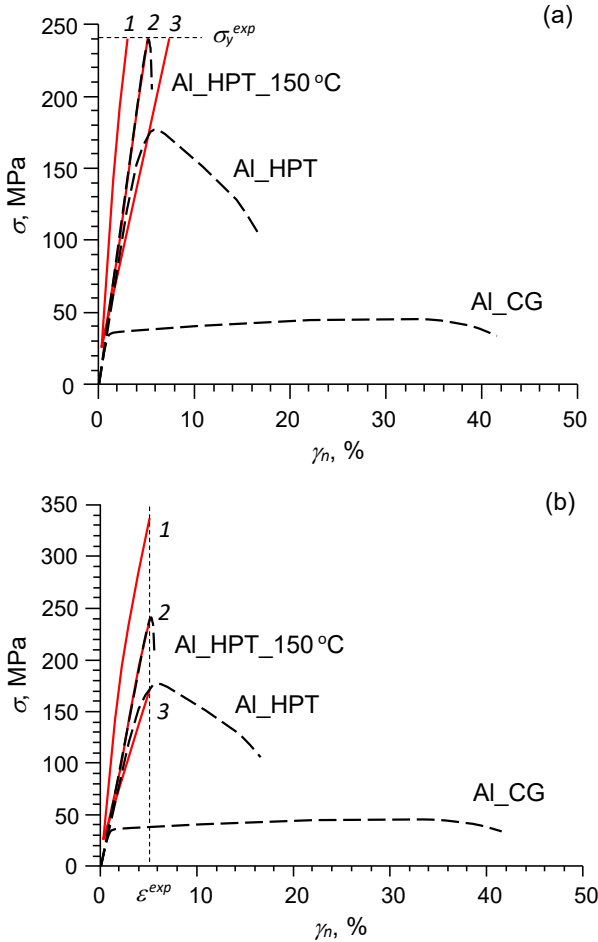


**Fig. 14.** Theoretical dependences (solid lines) of the flow stress  $\sigma$  on the plastic strain  $\gamma_n$  for the case of (a)  $\sigma \leq \sigma_y^{\text{exp}}$  and (b)  $\gamma_n \leq \varepsilon^{\text{exp}}$  with a different number of EGBDs in pile-ups:  $n_{pu} = 120$  (curve 1), 172 (2), and 250 (3) in comparison with (dashed lines) experimental data [19] for the initial coarse-grained technically pure Al (Al\_CG), UFG state obtained by HPT before annealing (Al\_HPT), and after annealing at 150 °C for 1 h (Al\_HPT\_150 °C). Adapted from Ref. [51].

number of EGBDs in pile-ups leads to a significant increase in plasticity and a reduction in strength, which corresponds to the case of UFG Al obtained by HPT and not subjected to heat treatment (annealing) (Fig. 14). From a comparison of theoretical dependences (solid curves) with experimental data from [19] (dashed curves), it is clear that the theoretical model proposed in [51] gives results that are in good agreement with the experiment for UFG Al obtained by HPT and then subjected to short-term low-temperature annealing [19] (curve 2 in Fig. 14), as well as for UFG Al obtained by the HPT without subsequent annealing (curve 3 in Fig. 14b).

Figure 15 shows the calculated in Ref. [52] dependences  $\sigma(\gamma_n)$  (solid curves) for the case of UFG aluminum after annealing and additional HPT deformation for various numbers of the EGBDs in the pile-ups:  $n_{pu} = 400$  (curve 1), 447 (2) and 500 (3). Here also the experimental

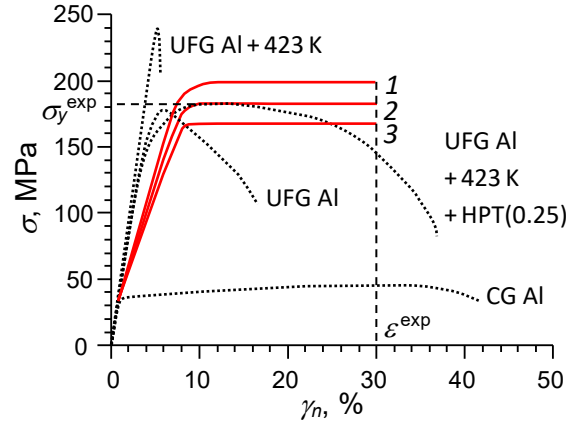


**Fig. 15.** Theoretical dependences (solid curves) of the flow stress  $\sigma$  on the plastic deformation value  $\gamma_n$  for various numbers of the EGBDs in pile-ups,  $n_{pu} = 400$  (curve 1), 447 (2) and 500 (3), in comparison with the experimental data [18] (dashed curves). Adapted from Ref. [52].

(dashed) curves for an initial coarse-grained Al (denoted as CG Al), UFG Al before annealing (denoted as UFG Al), UFG Al subjected to annealing only (denoted as UFG Al + 423 K) and UFG Al subjected to annealing and additional HPT deformation (denoted as UFG Al + 423 K + HPT(0.25)) are shown [18].

Since in this case, again there were no restrictions on the increase in the flow stress  $\sigma$ , therefore the plastic deformation value  $\gamma_n$  can increase until the EGBDs in the pile-ups finish. Thus, from agreement with experimental data [18], the authors of Ref. [52] applied a restriction on the maximum value of the plastic deformation  $\gamma_n = \varepsilon = 30\%$ , which corresponded to the flow stress  $\sigma = \sigma_{st}$  reaching saturation (Fig. 15). As is seen from Fig. 15, the value of the flow stress  $\sigma$  significantly increases at the initial stage of LD emission (the stage of hardening). At the next stage, after reaching a certain value  $\sigma_{st}$ , the value of the flow stress becomes practically independent of the number  $n$  of emitted LDs (the stage of stable plastic flow) (Fig. 15). This stage of the plastic deformation provides implementation of high ductility in UFG Al subjected to annealing and additional HPT deformation. At the same time, an increase of the number  $n_{pu}$  of the EGBDs in pile-ups leads to a decrease in the saturation value  $\sigma_{st}$  of the flow stress (Fig. 15). As it follows from Fig. 15, the theoretical results (curve 2) were in a good agreement with the experimental data [18] for UFG Al subjected to annealing and additional HPT deformation.

The aforementioned results concerned the AIH and DIS effects on UFG CP Al revealed in due course of RT mechanical tension. The influence of decreased deformation temperature  $T_{def}$  on the AIH effect for UFG Al was investigated for the first time in work [28] (see also Section 2 for details). In short, the authors studied the temperature dependences of the yield stress  $\sigma_{0.2}$ , ultimate tensile strength  $\sigma_{UTS}$ , uniform ductility  $\delta_1$  and total ducti-

lity  $\delta$  for the HPT-processed Al before and after annealing at 423 K for 1 h. They found that annealing-induced increase of  $\sigma_{0.2}$  and  $\sigma_{UTS}$  decreases with decreasing  $T_{def}$  and the AIH effect completely disappears at  $T_{def} \sim 193$  K and  $\sim 223$  K for  $\sigma_{0.2}$  and  $\sigma_{UTS}$ , respectively, whereas suppression of ductility by annealing is kept up to 193 K, at least. These results were discussed on the base of models [19,51,52] with assumption of thermally activated glide of EGBDs forming pile-ups at triple junctions of GBs, which emit LDs into grains. It was suggested that, when  $T_{def}$  decreases, the mobility of EGBDs exponentially drops [65] and they have no enough time  $t$  to form the EGBD pile-ups responsible for emission of LDs. As a result, LDs have to be emitted from various individual imperfections of GBs that needs higher level of applied stress, than that for LDs emission from EGBD pile-ups, and hence the overall yield stress must increase.

Let us consider the main points of the discussion in Ref. [28]. First, it seems evident that the lower  $T_{def}$ , the slower EGBDs and the weaker their pile-ups, the higher the yield stress must be. One can speculate that, at  $T_{def} = 77$  K, the thermally activated EGBD mobility becomes extremely low, and EGBDs could glide only under very high shear stress prevailing the Peierls stress  $\sigma_p$  characteristic for EGBDs [66]. This  $\sigma_p$  is expected to be much higher than that for LDs. For example, computer simulations [66] showed the upper bound  $\sigma_p \sim 0.0125G$ , where  $G$  is the shear modulus, for EGBDs in pure Fe. Applying this result to pure Al with  $G = 27$  GPa gives  $\sim 337.5$  MPa that is hardly available macroscopically in the tensile tests [28] with maximum shear stress  $\tau \approx \sigma_{UTS}(T_{def} = 77 \text{ K})/2 \approx 188$  MPa. Therefore, one can assume that, in this case, at  $T_{def} = 77$  K, the EGBDs are practically frozen in their positions. They cannot move, however, they can potentially emit LDs under local shear stress higher than some critical value.

Second, following the approach [65], the authors of Ref. [28] used a standard formula for velocity of thermally activated dislocation glide,

$$v = A(T)\tau \exp\left(-\frac{E}{kT}\right), \quad (2)$$

to estimate a characteristic time  $t$  necessary for the formation of an EGBD pile-up under an external shear stress  $\tau$  at a given temperature  $T$ . In the first approximation,

$$t \sim \alpha \frac{d_{av}}{v} = \alpha \frac{d_{av}}{A(T)\tau} \exp\left(\frac{E}{kT}\right), \quad (3)$$

where  $\alpha \sim 0.1$ ,  $E$  is the energy of kink formation and migration along the EGBD line, and  $k$  is the Boltzman constant. The temperature-dependent factor  $A(T)$  was chosen for the case of ‘high stresses and no obstacles, where there

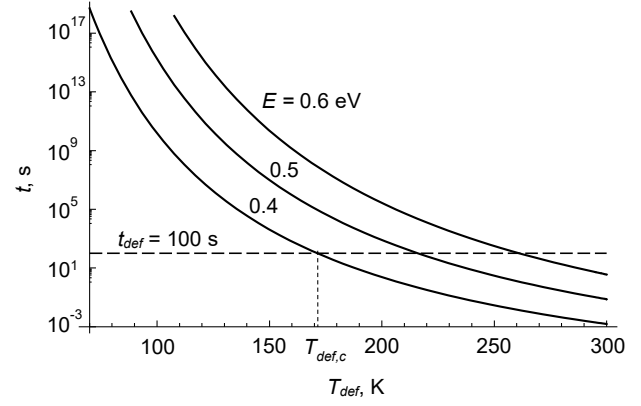


**Fig. 16.** Dependence of time  $t$  on the deformation temperature  $T_{def}$  for three different values of the activation energy  $E = 0.4, 0.5$  and  $0.6$  eV at  $\tau = 100$  MPa. Adapted from Ref. [28].

is no limitation on kinks propagation and kinks can propagate along dislocation until annihilation’ [41,65] as

$$A(T) = \frac{2b^3 s_v^2 v_D}{s_s kT}. \quad (4)$$

Here  $b$  is the Burgers vector magnitude of a EGBD,  $s_v$  is the distance between the stable positions of a kink along the EGBD line,  $v_D$  is the Debye frequency, and  $s_s$  is the distance between adjacent Peierls valleys within the GB. For numerical estimates, the authors [28] took  $d_{av} = 1000$  nm,  $\tau = 100$  MPa,  $v_D \approx 10^{13} \text{ s}^{-1}$ , and the values which were used for a special  $\Sigma 5$  GB in gold [65]:  $b = 0.13$  nm,  $s_v \approx 5b$ , and  $s_s \approx 10b$ . The biggest problem here was with a numerical value of  $E$  which was never determined for EGBDs in Al; see Ref. [28] for details.

With taking into account a great uncertainty in definition of the  $E$  value, the authors [28] plotted three curves  $t(T_{def})$  for three close values of  $E$ : 0.4, 0.5, and 0.6 eV (Fig. 16). At  $T_{def} = 293$  K, the curves show  $t \approx 0.002, 0.1$ , and 6 s, respectively, that is much smaller than a characteristic time of deformation  $t_{def} = 100$  s in the experiments [28], which is illustrated in Fig. 16 by the straight dashed line. This line crosses the curves  $t(T_{def})$  at the points corresponding to the values of a critical temperature  $T_{def,c}$  which conventionally separates the region of ‘normal’ temperatures ( $T_{def} > T_{def,c}$ ), in which the AIH effect is observable and well explained by the models [19,51], from the region of ‘low’ temperatures ( $T_{def} < T_{def,c}$ ), in which it is either not observed or not explained by the models [19,51]. For  $E = 0.4, 0.5$  and  $0.6$  eV, the cross points give  $T_{def,c} \approx 172, 216$  and  $263$  K. Coming back to their experimental plots in Fig. 10, the authors [28] concluded that the critical temperature region is indeed near 200 K. Therefore, the very rough estimate  $E = 0.4\text{--}0.5$  eV results in values of  $T_{def,c}$ , which are rather close to experimental data.

Thus, according to results reported in Ref. [28], the AIH effect becomes weaker and eventually totally disappears due to diminishing role of EGBD pile-ups in emission of LDs. It was shown that the characteristic time  $t$ , which is necessary for the formation of an EGBD pile-up, varies with the deformation temperature  $T_{def}$  as

$$t \sim T_{def} \exp\left(\frac{E}{kT_{def}}\right) \quad (5)$$

with  $E = 0.4\text{--}0.5$  eV, and the predicted critical temperature  $T_{def,c}$  of the AIH effect disappearance well corresponds to the experimental data [28].

### 3.2. The case of UFG Al–Cu–Zr alloy

It is well known that alloying of UFG Al with different doping elements (Cu, Mg, Zr, etc.) leads to strength increase (see Section 2). In particular, doping with Cu results in refinement of the grain structure [25,67,68] and strength increase [25,69] of aluminum-based alloys subjected to SPD. As was shown in experiments [10], the UFG Al–Cu–Zr alloy structured by HPT also demonstrates a significant increase in the strength characteristics while maintaining a functional ductility and good electrical conductivity. It is of interest that the AIH effect did not observed in this case, although a strong DIS effect was revealed [26].

Obviously, these peculiarities in mechanical behavior issue from the peculiarities of the microstructure of the UFG Al–Cu–Zr alloy. It is worth noting that the authors of Refs. [10,26] observed the formation of individual Cu-containing nanosized precipitates — nanoprecipitates of the  $\text{Al}_2\text{Cu}$  secondary phase ( $\text{Al}_2\text{Cu}$ -NPs) with sizes of 20–40 nm at GBs as a result of HPT processing of Al–Cu–Zr alloy. According to Ref. [10], the formation of such  $\text{Al}_2\text{Cu}$ -NPs at GBs contributes to a significant increase in the strength of the Al–Cu–Zr alloy, which is hard to explain by known strengthening mechanisms. As was shown in Ref. [10], the value of such additional strengthening related to the  $\text{Al}_2\text{Cu}$ -NPs at GBs is about 130 MPa that is comparable with the contribution from GB strengthening to the total strength of this alloy.

In this Section, we consider two recent theoretical models suggested for the UFG Al–Cu–Zr alloy [31,70]. The first one [70] was developed for describing the strengthening mechanism in the Al–Cu–Zr alloy due to the  $\text{Al}_2\text{Cu}$ -NPs at GBs, while the second one [31] explains the mechanism of the increase in plasticity of the UFG Al–Cu–Zr alloy after annealing and additional deformation. The departure point in this modeling was the assumption [19,28,51,52] that the key role in the plastic deformation of HPT processed UFG Al is played by EGBDs gliding along non-equilibrium GBs and forming

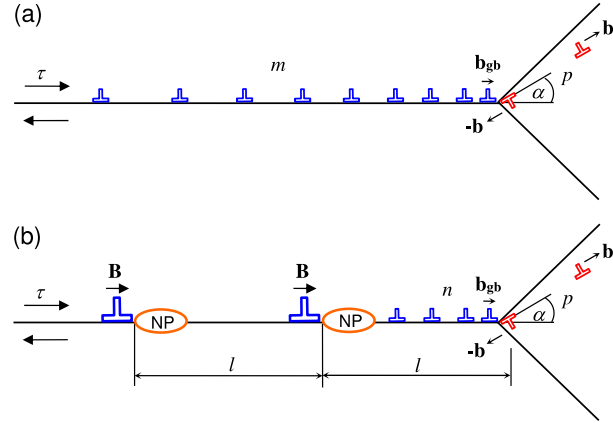


**Fig. 17.** Models of the lattice dislocation emission from the head of the pile-up of the EGBDs when (a) there is no NPs in the GB and (b) there are two NPs in the GB. Adapted from Ref. [70].

dislocation pile-ups at triple junctions of the GBs (see also Section 3.1). The critical stress required for the emission of LDs from the heads of such pile-ups to the bulk of neighboring grains, was considered as the flow stress of the UFG material [19,51,52]. Since in the Al–Cu–Zr alloy structured in a similar HPT route, new important elements of the non-equilibrium GB structure —  $\text{Al}_2\text{Cu}$ -NPs — appear, one can expect their strong interaction with EGBDs and new significant features in the behavior of the latter. Thus, the authors of Ref. [70] suggested a new theoretical model which reflected the interplay of EGBDs and  $\text{Al}_2\text{Cu}$ -NPs and allowed to estimate the contribution of  $\text{Al}_2\text{Cu}$ -NPs to strengthening of the UFG Al–Cu–Zr alloy.

Following Ref. [70], consider a single GB with an initial defect structure characterized by a pile-up of the EGBDs pressed by an external shear stress  $\tau$  to a triple junction of GBs (Fig. 17a). Such a dislocation pile-up can emit LDs from the triple junction into the adjacent grain. Let an edge LD with the Burgers vector  $\mathbf{b}$  (hereinafter called  $b$ -dislocation) be emitted from the head of the dislocation pile-up under the action of the external shear stress  $\tau$  and glide along a crystallographic plane that makes the angle  $\alpha$  with the GB plane. In terms of the continuum approach, the emission of the  $b$ -dislocation can be represented as formation of a dipole of the LDs with Burgers vectors  $\pm\mathbf{b}$  (Fig. 17a).

According to the model [70], the aforementioned  $\text{Al}_2\text{Cu}$ -NPs act as obstacles for the slip of the EGBDs. Thus, the appearance of the  $\text{Al}_2\text{Cu}$ -NPs in Al–Cu–Zr alloy structured by HPT leads to formation of a new defect structure in the GB, which is characterized by  $N$   $\text{Al}_2\text{Cu}$ -NPs periodically distributed along the GB with a period  $l$ , and  $N + 1$  identical pile-ups of EGBDs pressed by an external shear stress  $\tau$  to the NPs and to the triple junction of the GBs (Fig. 17b). For the sake of simplicity, the dislocation pile-ups at the NPs were modeled by edge superdislocations with Burgers vector  $\mathbf{B}$  ( $B$ -superdislocations). The

magnitudes of the superdislocation Burgers vectors are supposed to be the same,  $B = nb_{gb}$ , where  $n$  is the number of the EGBDs in each dislocation pile-up (Fig. 17b), and  $b_{gb}$  is the magnitude of the Burgers vector of an EGBD.

Within the model [70], the combined action of the external shear stress  $\tau$  and the shear stress field created by the superdislocations at the NPs leads to the emission of the lattice  $b$ -dislocation from the triple junction of the GBs. The emission event was modeled as the formation of the corresponding  $\pm b$ -dislocation dipole (Fig. 17b).

The dislocation emission process was specified in Ref. [70] by the energy difference:

$$\Delta W = E_{self}^{bb} + E_{int}^{B-bb} + E_{int}^{pu-bb} + E_{int}^{\tau}, \quad (6)$$

where  $E_{self}^{bb}$  is the self-energy of the  $\pm b$ -dislocation dipole,  $E_{int}^{B-bb}$  is the sum interaction energy of the  $B$ -superdislocations at the NPs and the  $\pm b$ -dislocation dipole,  $E_{int}^{pu-bb}$  is the sum interaction energy between  $n$  EGBDs in the pile-up at the triple junction of the GBs and the  $\pm b$ -dislocation dipole, and  $E_{int}^{\tau}$  denotes the interaction energy of the applied shear stress  $\tau$  with the  $\pm b$ -dislocation dipole. All these energy terms are given in Ref. [70].

The authors of Ref. [70] numerically analyzed the dependence of  $\Delta W$  on characteristics of the system under consideration in the exemplary case of the UFG Al–Cu–Zr alloy with the average grain size  $d \approx 300$  nm [10]. First, the dependences of  $\Delta W$  on the distance  $p$  moved by the  $b$ -dislocation in the grain interior were calculated for different values of the external shear stress  $\tau$  at the following typical values of the system parameters [41,63]:  $G = 27$  GPa,  $\nu = 0.33$ ,  $a = 0.405$  nm,  $b = a\sqrt{2}/2$ ,  $b_{gb} = 0.1$  nm, and  $l = d/(N+1)$ . The emission angle  $\alpha$  was chosen as the average angle  $\alpha = 22^\circ$  between  $0^\circ$  and  $45^\circ$  that corresponds to the maximum and minimum levels of the external shear stress  $\tau$ , respectively. The total number of EGBDs in all the cases under investigation was taken as  $m = (N+1)n = 36$ . This value well corresponds to the typical length of GBs in experiments [22] and allowed to obtain the results well meeting the levels of the flow stress measured in Ref. [10]. The shear stress  $\tau$  was related to the flow stress  $\sigma$  as follows:  $\sigma = 2\tau/\cos 2\alpha$ . The curves  $\Delta W(p)$  are shown in Fig. 18 for different values of the flow stress  $\sigma$  at  $n = 36$ , 18, and 12 in the cases of no NPs ( $N = 0$ , Fig. 18a), one NP ( $N = 1$ , Fig. 18b), and two NPs ( $N = 2$ , Fig. 18c), respectively, in the GB that corresponds to direct experimental observations of Al<sub>2</sub>Cu-NPs in Ref. [10].

As is seen, for  $N = 0, 1$ , and  $2$ , the critical value of the flow stress  $\sigma = \sigma_c$ , under which the dislocation emission becomes energetically favorable ( $\Delta W = 0$  at  $p = 1$  nm and  $\partial\Delta W/\partial p < 0$  at  $p > 1$  nm), is equal to 320, 450, and 680 MPa, respectively (see the red curves in Fig. 18). To explain these results, the authors [70] calculated the sum shear stress  $\tau_{sum}$  in front of the pile-up, at

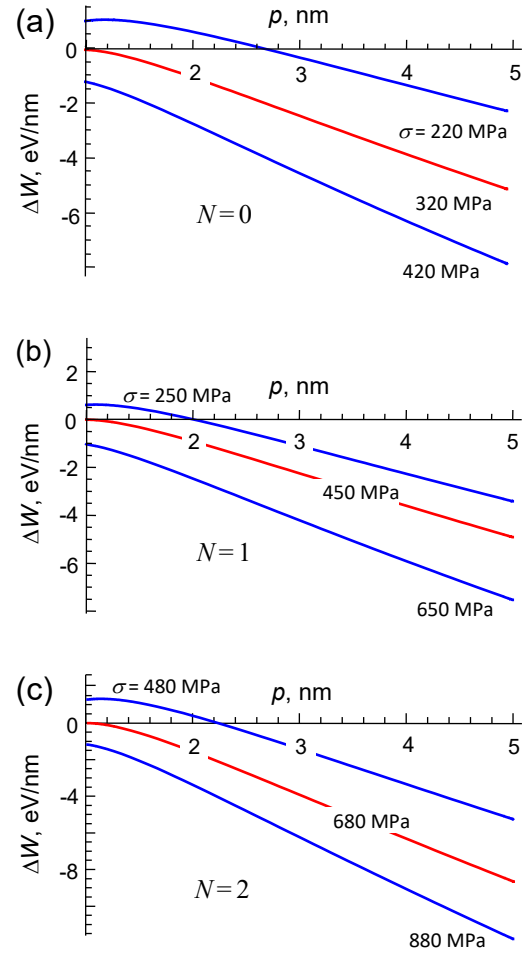


**Fig. 18.** Dependences of the energy difference  $\Delta W$  on the distance  $p$  for different values of the flow stress  $\sigma$  and the number of the EGBDs in the pile-ups: (a)  $n = 36$ , (b) 18, and (c) 12 in the cases of  $N = 0, 1$ , and  $2$ , respectively. The red curves correspond to the critical values of the flow stress under which the dislocation emission becomes energetically favorable. Adapted from Ref. [70].

$\alpha = 0$  and at the distance 1 nm from the head EGBD — just in the emission region — for the three cases: (i)  $N = 0$ ,  $\sigma = 320$  MPa, (ii)  $N = 1$ ,  $\sigma = 450$  MPa, and (iii)  $N = 2$ ,  $\sigma = 680$  MPa. The results were  $\tau_{sum} \approx 2.83$  GPa in case (i), 2.78 GPa in case (ii), and 2.79 GPa in case (iii) that is roughly 2.8 GPa in all the three cases. This value is approximately equal to  $G/10$  that is of the order of magnitude of the theoretical shear strength.

The dependence of the critical flow stress  $\sigma_c$  on the number  $N$  of the NPs in the GB is shown in Fig. 19. It is seen that  $\sigma_c$  noticeably increases with  $N$  and the discrete dependence  $\sigma_c(N)$  is very close to linear. To determine the best-fitting line approximating the calculated points, the authors [70] used the method of least squares. In the framework of this method, the equation of the best-fitting line for the dependence  $\sigma_c(N)$  is given in units of GPa as follows [70]:

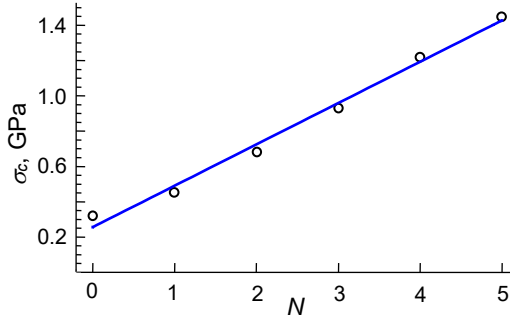


**Fig. 19.** Dependence of the critical flow stress  $\sigma_c$  on the number  $N$  of the NPs. The calculated points (open circles) are approximated by the best-fitting straight line. Adapted from Ref. [70].

$$\sigma_c \approx 0.255 + 0.235N. \quad (7)$$

The corresponding linear dependence  $\sigma_c(N)$  is shown by the solid line in Fig. 19. This result can be used for rough estimates of the expected YS of the UFG Al–Cu–Zr alloy with Al<sub>2</sub>Cu-NPs in GBs, depending on the average number of NPs at the boundary.

Thus, the authors [70] showed that, in the case of no NPs in GBs, the critical flow stress was about of 320 MPa. It well corresponds to the value of the yield stress  $\sigma_{0.2}$  estimated on the basis of experimentally determined microstructural parameters as the sum of contributions from known strengthening mechanisms, such as the Peierls–Nabarro hardening, the solid solution hardening, the strain hardening, the GB hardening and the dispersion hardening [10]. In contrast, in the case with one Al<sub>2</sub>Cu-NP in a GB, it is about 450 MPa in accordance with measurements in Ref. [10]. Therefore, the difference in 130 MPa was attributed to the role of Al<sub>2</sub>Cu-NPs as obstacles for glide of EGBDs in non-equilibrium GBs typical for HPT processed metals and alloys. This difference characterizes the value of the additional hardening of the UFG Al–Cu–Zr alloy structured by HPT and demonstrates good agreement with experimental data [10]. The authors [70] also noted that, in the HPT processed Al–Zr alloy, in which GBs did not contain any precipitates of secondary phase, the theoretically calculated value of  $\sigma_{0.2}$  as the sum of known strengthening mechanisms well corresponds to the experimental value of the YS [22].

Thus, a theoretical model of new micromechanism of strengthening in the UFG Al–Cu–Zr alloy was developed in [70]. In the model, the formation of Al<sub>2</sub>Cu-NPs at GBs, which act as obstacles for EGBD slip, leads to a significant increase in the strength of the Al–Cu–Zr alloy. The deformation mechanism realized through the emission of LDs from the heads of the pile-ups of the EGBDs near the triple junctions of the GBs. It was shown that the division of gliding EGBDs into separate pile-ups by Al<sub>2</sub>Cu-NPs can provide additional hardening of the UFG Al–Cu–Zr alloy

structured by HPT, the value of which well corresponds to experimental measurements [10].

In spite of high strength of the UFG Al–Cu–Zr alloy structured by HPT, its plasticity drastically reduced to 3–5% [10]. To cope with this problem, a subsequent thermomechanical treatment was used, which included low temperature annealing and slight additional HPT deformation. This treatment significantly increased the ductility of the UFG alloy while maintaining its strength at a high level [26], although the intermediate annealing catastrophically reduced the plasticity of this material to a practically brittle state with a slight decrease in strength [26]. It was also noted in Refs. [26,27] that nanoscopic precipitates of Al<sub>2</sub>Cu-NPs in GBs increased after annealing (and remained after additional deformation) in size up to values of the order of 60 nm and acquired a faceting, i.e., they transformed from ellipsoidal into faceted polyhedral ones. In this case, it was natural to assume that edges appeared on them, which became powerful concentrators of both intrinsic and applied stresses, capable of efficiently emitting LDs. The ability of NPs to emit LDs was also confirmed by computer simulations [71,72].

In addition, it is well known that HPT leads to an increase in the number of EGBDs. This was also observed in Ref. [26], where it was noted that after a slight additional (after annealing) HPT, the dislocation density increased by a factor of 1.8. Thus, as a result of the action of additional HPT on annealed samples of UFG Al–Cu–Zr alloy, important structural changes should occur in them [31]: (i) GBs should be saturated with EGBDs; (ii) during subsequent loading, the sliding EGBDs should pile up near the NPs, which become effective obstacles for the sliding of the EGBDs, and (iii) under the influence of the pile-ups of EGBDs, these NPs, grown and faceted as a result of annealing, should themselves become effective sources of LDs, the emission of which into adjacent grains should provide a significant increase in the ductility of the UFG alloy.

Based on the above assumptions (i)–(iii), the authors of Ref. [31] suggested a theoretical model that was aimed at explaining the increase in the ductility of the UFG Al–Cu–Zr alloy structured by HPT and then subjected to low-temperature annealing and a small additional HPT, experimentally established in Ref. [26]. In the framework of this model, the main mechanism of plastic deformation was considered to be the emission of LDs by the edges of Al<sub>2</sub>Cu-NPs placed in GBs.

Following the authors of Ref. [31], consider a separate NP in a GB, modeled by the inclusion of a rectangular shape ABCD, the sizes of which are given by the diagonal  $h$  and the angle of inclination  $\alpha$  of the BC face to the GB plane (Fig. 20). It is known [73–77] that the formation of lamellar Al<sub>2</sub>Cu-NPs in Al-based alloys

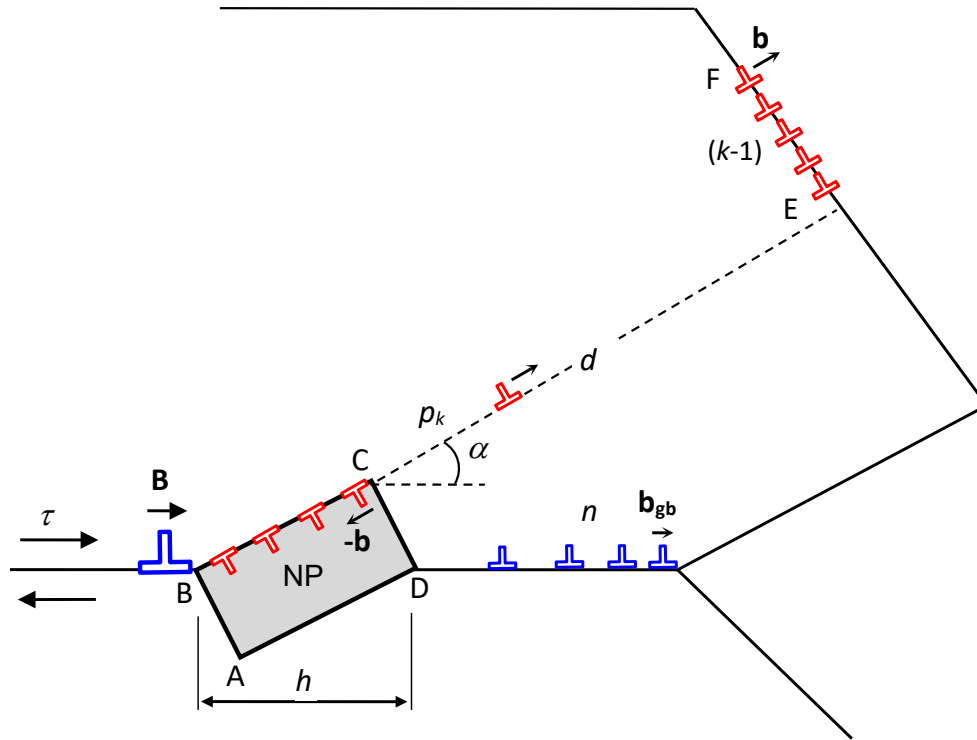


**Fig. 20.** Model of the emission of the  $k$ -th LD from the corner C of the rectangular NP ABCD and completion of the wall EF from  $k - 1$  climbing  $b$ -dislocations. Adapted from Ref. [31].

supersaturated with copper occurs in such a way that the larger faces of the  $\text{Al}_2\text{Cu}$ -NP lie in the  $\{111\}$  planes of the aluminum matrix, and, in most cases, the orientational relations are  $(110)_{\text{Al}_2\text{Cu}} \parallel (111)_{\text{Al}}$ ,  $[1\bar{1}0]_{\text{Al}_2\text{Cu}} \parallel [10\bar{1}]_{\text{Al}}$  and  $[001]_{\text{Al}_2\text{Cu}} \parallel [1\bar{2}1]_{\text{Al}}$ . This is explained [77] by the relatively low lattice mismatch  $f$  at such a boundary in the  $[1\bar{1}0]_{\text{Al}_2\text{Cu}} \parallel [10\bar{1}]_{\text{Al}}$  ( $f = 1.23\%$ ) and  $[001]_{\text{Al}_2\text{Cu}} \parallel [1\bar{2}1]_{\text{Al}}$  ( $f = 1.71\%$ ) directions, as well as by the growth kinetics of the  $\text{Al}_2\text{Cu}$  intermetallic, whose  $\{110\}$  faces grow faster than the others [73]. Note that recent works on computer simulation of the structure and properties of such interfaces in lamellar eutectic Al- $\text{Al}_2\text{Cu}$  composites [75,76] have shown that they relatively easily transit from a coherent state to a semicoherent one due to the filling of the interfaces with three families of misfit dislocations (MDs) by sliding along the interface of partial Shockley dislocations. Such a structure of the interface allows it to act as a plane of relatively easy interfacial slip due to the motion of the MDs [75].

For definiteness, the authors of Ref. [31] assumed that the NP boundaries were initially in a coherent state, that is, they did not contain MDs. It was further assumed that the GB under consideration contained pile-ups of EGBDs pressed against the NP and the triple junction of GBs. In this case, the pile-up in front of the NP was modeled by an edge superdislocation with the Burgers vector  $\mathbf{B}$  (hereinafter  $B$ -superdislocation) equal in absolute value to  $B = b_{gb}n$ , where  $b_{gb}$  is the modulus of the Burgers vector

of an individual EGBD and  $n$  is the number of EGBDs in the pile-up.

Within the framework of such a model, it is natural to assume that in the sum field of shear stresses — the applied stress  $\tau$ , the stress field of the NP, and the stress field of the  $B$ -superdislocation — an LD with the Burgers vector  $\mathbf{b}$  (hereinafter  $b$ -dislocation) is emitted from the corner C of the NP into the neighboring grain (Fig. 20).

Based on the results of experimental observations and computer simulations of the  $\text{Al}_2\text{Cu}$  NPs in aluminum alloys [73–77], the authors of Ref. [31] assumed that the easy slip plane of LDs coincided with the plane of the BC face and made an angle  $\alpha$  with the GB plane. The emission of such a  $b$ -dislocation was represented as the nucleation of an LD dipole with Burgers vectors  $\pm\mathbf{b}$  (Fig. 20). The authors [31] considered the mechanism of successive emission of LDs from the NP edge, similar to that proposed earlier in Ref. [52] (see also Subsection 3.1). For definiteness, the emitted LD was considered as a positive dislocation of the formed dipole. As before in the model [52], the emitted positive LD crossed the grain, reached the opposite GB, and was captured by it. Then the next positive LD was emitted, which also crossed the grain and was captured by the opposite GB, along which the previous LD climbed from the point of its capture by the GB. As a result of such a successive emission of positive LDs and their capture by the opposite GB, a wall of climbing EGBDs was formed, which, with its stress field, made subsequent LD

emissions difficult [52]. Applying this approach to their case, the authors [31] obtained a defect structure in the form of the  $k$ -th LD emitted from the NP edge and the wall EF from  $k - 1$  climbing  $b$ -dislocations (Fig. 20).

Within the model, it was also assumed that negative dislocations ( $-b$ -dislocations) of the nucleating LD dipoles glided in the opposite direction from the emission point and formed a periodic row along the face BC (Fig. 20), acting as MDs in accordance with computer simulation data [75,76]. Similar models of the formation of MDs have recently been studied in relation to composite nanostructures, i.e., nanowires of rectangular cross section in nanolayers [78] and in cylindrical nanowires [79]. The formation of such a row of MDs, on the one hand, reduces the stress field of the NP and increases the total energy gain caused by the emission of the LDs due to a decrease in the strain energy of the NP, and on the other hand, reduces the total shear stress acting on the emitted LDs, and thereby reduces the total gain in the energy of the system. To simplify the model, the authors [31] assumed that such a decrease in the overall gain in energy from a decrease in the shear stress acting on the emitted LDs was approximately compensated by an additional gain in the strain energy of the NP, which made it possible, in the first approximation, not to take into account the effect of  $-b$ -dislocations on the LD emission.

To simplify the calculations, the authors [31] also neglected the effect of the stress field of the pile-up of the EGBDs near the triple junction on the LD emission. Indeed, the main part of dislocations of the pile-up is concentrated in its head at the triple junction and is located at a considerable distance from the point of LD emission, and the critical conditions for this emission are already determined at a small (on the order of 1 nm) LD displacement from point C. They also neglected the difference in the elastic moduli of the NP and the surrounding grains, thus assuming the alloy material to be an elastically isotropic homogeneous medium.

As an elastic model of NP, the authors [31] took a dilatation inclusion in the form of a long parallelepiped oriented with its longitudinal axis perpendicularly to the plane of Fig. 20. The elastic fields of such an inclusion are determined by its shape and its own homogeneous three-dimensional dilatation eigenstrain  $\varepsilon^*$  (see, for example, Refs. [80,81]). In turn, the value of  $\varepsilon^*$  is determined by the misfit  $f$  in the lattice parameters of the NP and the surrounding alloy, the difference in their thermal expansion coefficients, and the difference in annealing and mechanical testing temperatures.

In accordance with the model [31], the emission of the  $k$ -th LD from the NP (Fig. 20) is characterized by the energy difference  $\Delta W_k$  as follows:

$$\Delta W_k = E_k^{2b} + E_k^{NP-2b} + E_k^{B-2b} + E_k^{b-2b} + E_k^\tau, \quad (8)$$

where  $E_k^{2b}$  is the self-energy of the  $k$ -th dipole of  $\pm b$ -dislocations,  $E_k^{NP-2b}$  is the interaction energy between the NP ABCD and the  $k$ -th dipole of  $\pm b$ -dislocations,  $E_k^{B-2b}$  is the interaction energy between the  $B$ -superdislocation ahead of the NP and the  $k$ -th dipole of  $\pm b$ -dislocations,  $E_k^{b-2b}$  is the interaction energy between the  $k$ -th dipole of  $\pm b$ -dislocations and the wall EF of  $k - 1$  climbing  $b$ -dislocations, and  $E_k^\tau$  is the interaction energy of the applied shear stress  $\tau$  with the  $k$ -th dipole of  $\pm b$ -dislocations. These energy terms are given in Ref. [31].

Calculated these terms, the authors [31] found the critical stress  $\tau_{c(k)}$  which was defined as the minimum shear stress required to cross the grain by the  $k$ -th emitted LD (when  $p_k = d$ , see Fig. 20). This stress was calculated from the conditions [52]  $\Delta W_k(p_k = p') = 0$ ,  $\Delta W_k|_{p_k > p'} < 0$  and  $\partial \Delta W_k / \partial p_k|_{p_k > p'} < 0$ , where  $p' = 1$  nm. It was related to the flow stress  $\sigma$  by the following relationship:  $\sigma = 2\tau_{c(k)} / \cos 2\alpha$ . To estimate the degree of plastic deformation that the emitted LDs made, the authors [31] used the well-known relation [52]  $\varepsilon \approx kb / d$ .

With these estimates for the flow stress  $\sigma$  and the plastic deformation degree  $\varepsilon$ , they calculated the dependences  $\sigma(\varepsilon)$  for the cases of the UFG Al–Cu–Zr alloy after HPT treatment, low-temperature annealing, and additional small HPT treatment. The calculations were carried out for the following values of the defect structure parameters [41,63]:  $G = 27$  GPa,  $\nu = 0.33$ ,  $a = 0.405$  nm,  $b = a\sqrt{2} / 2$ ,  $b_{gb} = 0.1$  nm, and  $d \approx 300$  nm [26]. The angle  $\alpha = 22^\circ$  was chosen as the average between the angles  $0^\circ$  and  $45^\circ$  which correspond to the maximum and minimum levels of the external shear stress  $\tau$ . The number of EGBDs in front of the NP was chosen to be  $n = 18$  (this corresponds to the case of one NP from the theoretical work [70]). For dilatation eigenstrain of NPs, the authors [31] took the average value of the lattice misfit between the aluminum matrix and  $\text{Al}_2\text{Cu}$ -NP in two orthogonal directions at the interface  $(110)_{\text{Al}_2\text{Cu}} \parallel (111)_{\text{Al}}$  [77]:  $\varepsilon^* = f \approx (0.0123 + 0.0171) / 2 = 0.0147$ . In this case, the contribution from the difference in the thermal expansion coefficients was neglected because of its relative smallness (on the order of  $\Delta\alpha\Delta T = (\alpha_{\text{Al}} - \alpha_{\text{Al}_2\text{Cu}})(T_{\text{AN}} - T_{\text{room}}) \approx (27 - 20) \cdot 10^{-6} (398 - 300) \approx 6.86 \cdot 10^{-4}$ , where  $\alpha_{\text{Al}}$  and  $\alpha_{\text{Al}_2\text{Cu}}$  are the thermal expansion coefficients of Al and  $\text{Al}_2\text{Cu}$ ,  $T_{\text{AN}}$  is the annealing temperature, and  $T_{\text{room}}$  is room temperature).

The calculated in Ref. [31] dependences  $\sigma(\varepsilon)$  (blue dashed curves) are shown in Fig. 21 for different values of the NP size  $h$  in comparison with the experimental data [26] for the UFG Al–Cu–Zr alloy in various states: aged alloy (black curve, AG), aged alloy after HPT treatment (red curve, AG + HPT), aged alloy after HPT treatment and additional low-temperature annealing at  $T_{\text{AN}} = 125$  °C, 4 h (green curve, AG + HPT + AN), and

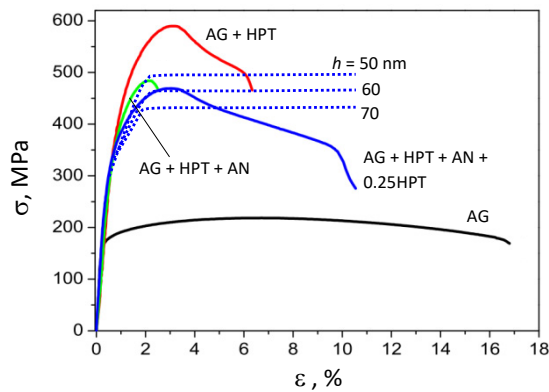


**Fig. 21.** Theoretical dependences (dashed curves) of the flow stress  $\sigma$  on the value of plastic deformation  $\varepsilon$  for different sizes  $h$  of the NP. For comparison, the experimental dependences  $\sigma(\varepsilon)$  (solid curves) of the UFG Al–Cu–Zr alloy at different stages of its thermo-mechanical treatment are presented. Adapted from Ref. [31].

aged alloy after HPT treatment, additional low-temperature annealing at  $T_{AN} = 125$  °C, 4 h and a small additional HPT (solid blue curve, AG + HPT + AN + 0.25HPT). As is seen from Fig. 21, the theoretical dependences  $\sigma(\varepsilon)$  at the initial stage of LD emission demonstrate a significant increase in the flow stress, and at the next stage, after reaching a certain value of the flow stress  $\sigma = \sigma_{st}$ , they reach saturation and practically do not depend on the number of emitted LDs. This stage of plastic deformation characterizes the increase in the plasticity of the UFG alloy after additional HPT treatment.

A comparison of the theoretical dependences with the experimental ones showed that the theoretical curve corresponding to the NP size  $h = 60$  nm demonstrates the best agreement with the experiment, which is in good agreement with the experimental data [26]. The authors of Ref. [31] noted that within their model there was no restriction on the growth of the flow stress. Therefore, the value of plastic deformation also constantly increased, which does not correspond to reality. Thus, relying on the experimental data [26], a limitation was artificially introduced for the value of plastic deformation  $\varepsilon = 11\%$  which corresponds to the flow stress that has reached saturation,  $\sigma = \sigma_{st}$ .

Thus, the theoretical model [31] describes the increase in the ductility of the UFG Al–Cu–Zr alloy after HPT treatment, additional low-temperature annealing, and additional small HPT treatment. Within the model, this increase in ductility is due to the emission of LDs by the edges of faceted Al<sub>2</sub>Cu-NPs formed at GBs during the thermomechanical treatment of the alloy. The obtained estimates of the flow stress and degree of plastic deformation demonstrate good agreement with the experimental data [26]. The authors [31] concluded that the emission of LDs by NP edges provides higher plasticity compared to the emission of LDs from triple junctions of GBs, since in the case of NPs there

are no restrictions on the number of emitted LDs, in contrast to their emission from triple junctions of GBs, when the number of emitted LDs is limited by the number of EGBDs in pile-ups at the triple junctions. In addition, in the case of a UFG alloy that has undergone additional low-temperature annealing and an additional minor HPT treatment, in contrast to the UFG alloy after low temperature annealing, there is a sufficient amount of EGBDs in the GBs to ensure the operation of Al<sub>2</sub>Cu-NPs as sources of LDs in a larger number of grains. All this, in the authors' opinion, determines the high ductility of the UFG Al–Cu–Zr alloy after additional HPT treatment.

## 5. SUMMARY AND CONCLUSIONS

A brief review of recent experimental observations and theoretical modeling of the effects of annealing induced hardening (AIH) and deformation induced softening (DIS) of ultrafine-grained (UFG) Al and Al-based alloys structured by high pressure torsion (HPT) has been presented. The influence of the temperature of mechanical testing and the alloying elements on these effects has been considered. A number of theoretical models aimed at the revealing the origin of the AIH and DIS effects and their dependence on the testing temperature and alloy content has been discussed in detail.

Based on the experimental and theoretical results, one can make the following conclusions:

- In UFG commercially pure (CP) Al structured by SPD methods, the manifestation and magnitude of AIH effect strongly depend on parameters of initial UFG structure. In CP Al structured by ARB, the annealing-induced increase of yield stress is equal to  $\sim 9\%$ , whereas in CP Al structured by HPT processing, it exceeds 50% under similar conditions of annealing.
- Relaxation of HAGBs during annealing which is accompanied by decrease in dislocation density in them plays key role in AIH effect in HPT-processed Al. The activation energy of the process underlying hardening by annealing has been determined for HPT-processed CP Al. The obtained value  $Q_a \approx 57$  kJ·mol<sup>-1</sup> is well comparable with the energy of GB self-diffusion in aluminum. Restoration or even increase of dislocation density in HAGBs by small additional HPT deformation is responsible for the DIS effect in HPT-processed Al.
- The change of type of additional deformation after annealing of HPT-processed Al from HPT to CR leads to suppression of the DIS effect despite resulting comparable increase of dislocation density. Unlike to additional HPT deformation, additional CR deformation introduces additional dislocation density mainly in grain interior in Al structured by HPT.

- The HPT-processed Al–0.4Zr alloy also demonstrates drastic AIH and DIS effects. The doping by Zr expands the temperature range of existence of the AIH effect to 280 °C with to the peak-effect at 230 °C.
- Doping by Cu (HPT-processed Al–Cu and Al–Cu–Zr alloys) suppresses manifestation of the AIH effect, whereas additional small HPT deformation after annealing results in drastic increase of plasticity (by nearly 4 times) — the DIS (or PE) effect.
- The magnitudes of AIH and DIS effect in HPT-processed Al and Al–0.4Zr alloy and the DIS (or PE) in HPT-processed Al–1.47Cu–0.34Zr alloy gradually decreases with decreasing of tensile test temperature  $T_{def}$  and disappears at  $T_{def} = 193–223$  K.
- In the temperature range of manifestation of the AIH and DIS effects, the value of activation energy  $Q$  of plastic flow decreases several times after annealing in HPT-processed Al and Al–0.4Zr alloy and restores to that before annealing after additional HPT deformation. In HPT-processed Al–1.47Cu–0.34Zr alloy, the  $Q$ -values are different in all three states (before and after annealing, after annealing with additional HPT deformation).
- The absence of the AIH effect and manifestation of the drastic DIS effect in the HPT-processed Al–Cu–Zr alloy are related to the change of GB structural parameters (the size and shape of Al<sub>2</sub>Cu nanoprecipitates and the dislocation density). The other microstructural parameters are nearly unchanged after annealing and additional deformation.
- The magnitude of the DIS (PE) effect in HPT-processed Al–1.47Cu–0.34Zr alloy does not depend on the strain rate of tensile test in the range from  $10^{-4}$  s<sup>-1</sup> to  $10^{-3}$  s<sup>-1</sup> and decreases rapidly with further increase of the strain rate.
- In UFG CP Al structured by HPT, the AIH and DIS effect can be explained by drastic changes in the number of extrinsic grain-boundary dislocations (EGBDs) capable to glide within non-equilibrium GBs and form the dislocation pile-ups at triple junctions of the GBs. When the shear stress  $\tau$  acting on the head EGBD in such a pile-up exceeds a critical value  $\tau_c$ , the head EGBD starts emitting lattice dislocations (LDs) in the neighboring grain, thus providing local plastic deformation.
- After low-temperature annealing of the HPT treated Al, the number of gliding EGBDs becomes so small that they can form rather ‘weak’ pile-ups which require a relatively high level of  $\tau$  to reach the critical stress  $\tau_c$  for starting the emission of LDs. This explains the AIH effect in UFG CP Al.
- After subsequent additional small plastic deformation of the HPT treated and annealed Al, the number of gliding EGBDs increases so much that they can form rather ‘strong’ pile-ups which require a relatively low level of  $\tau$  to reach the critical stress  $\tau_c$  for the LD emission and can emit much more LDs than after annealing. This explains the DIS effect in UFG CP Al.
- A decrease in the temperature of mechanical testing of the UFG CP Al exponentially increases the time of creation of EGBD pile-ups, thus blocking the above scenarios of the LD emission from the GB triple junctions. As a result, the AIH effect becomes weaker and eventually totally disappears with diminishing temperature of mechanical testing.
- In the Al–Cu–Zr alloy structured in a similar HPT route, new important elements of the non-equilibrium GB structure — Al<sub>2</sub>Cu nanoprecipitates (NPs) — appear, which can strongly interact with EGBDs and provide new significant features in the mechanical behavior of the alloy. In particular, the interplay of EGBDs and Al<sub>2</sub>Cu-NPs can give a significant contribution to strengthening of the UFG Al–Cu–Zr alloy.
- Although the AIH effect has not been revealed in experiments with the UFG Al–Cu–Zr alloy, the additional thermo-mechanical treatment of the alloy, including low-temperature annealing and additional small HPT, leads to a significant increase in its ductility. As is shown theoretically, this increase in the ductility of the alloy can be explained by the emission of LDs from the edges of faceted Al<sub>2</sub>Cu-NPs formed at GBs during the thermo-mechanical treatment.
- In general, the physical origin of the AIH and DIS effects in UFG Al and Al-based alloys structured by HPT is in the transformations of the defect structure (EGBDs and NPs) of GBs in the process of low temperature annealing and subsequent small plastic deformation of the UFG materials.

## REFERENCES

- [1] K. Edalati, A. Bachmaier, V.A. Beloshenko, Y. Beygelzimer, V.D. Blank, W. Botta, et al., *Nanomaterials by severe plastic deformation: review of historical developments and recent advances*, Mater. Res. Lett., 2022, vol. 10, no. 4, pp. 163–256.
- [2] I. Sabirov, M.Y. Murashkin, R.Z. Valiev, *Nanostructured aluminium alloys produced by severe plastic deformation: new horizons in development*, Mater. Sci. Eng. A, 2013, vol. 560, pp. 1–24.
- [3] R.Z. Valiev, M.Yu. Murashkin, I. Sabirov, *A nanostructural design to produce high-strength Al alloys with enhanced electrical conductivity*, Scr. Mater., 2014, vol. 76, pp. 13–16.
- [4] I. Sabirov, M.R. Barnett, Y. Estrin, P.D. Hodgson, *The effect of strain rate on the deformation mechanisms and the strain rate sensitivity of an ultra-fine-grained Al alloy*, Scr. Mater., 2009, vol. 61, no. 2, pp. 181–184.

- [5] C.-F. Yang, J.-H. Pan, T.-H. Lee, *Work-softening and anneal-hardening behaviors in fine grained Zn–Al alloys*, *J. Alloys Compd.*, 2009, vol. 468, no. 1–2, pp. 230–236.
- [6] A.S. Khan, J. Liu, *A deformation mechanism based crystal plasticity model of ultrafine-grained/nanocrystalline FCC polycrystals*, *Int. J. Plast.*, 2016, vol. 86, pp. 56–69.
- [7] H. Van Swygenhoven, *Footprints of plastic deformation in nanocrystalline metals*, *Mater. Sci. Eng. A*, 2008, vol. 483–484, no. 1, pp. 33–39.
- [8] F. Momprou, D. Caillard, M. Legros, H. Mughrabi, *In situ TEM observations of reverse dislocation motion upon unloading in tensile-deformed UFG aluminium*, *Acta Mater.*, 2012, vol. 60, no. 8, pp. 3402–3414.
- [9] X. Sauvage, G. Wilde, S.V. Divinski, Z. Horita, R.Z. Valiev, *Grain boundaries in ultrafine grained materials processed by severe plastic deformation and related phenomena*, *Mat. Sci. Eng. A*, 2012, vol. 540, pp. 1–12.
- [10] T.S. Orlova, D.I. Sadykov, M.Yu. Murashkin, V.U. Kazykhanov, N.A. Enikeev, *Peculiarities of strengthening of Al–Cu–Zr alloy structured by severe plastic deformation*, *Phys. Solid State*, 2021, vol. 63, no. 12, pp. 1744–1756.
- [11] T.S. Orlova, T.A. Latynina, M.Yu. Murashkin, F. Chabanaï, L. Rigutti, W. Lefebvre, *Effects of Mg on strengthening mechanisms in ultrafine-grained Al–Mg–Zr alloy*, *J. Alloys Compd.*, 2021, vol. 859, art. no. 157775.
- [12] X. Huang, N. Hansen, N. Tsuji, *Hardening by annealing and softening by deformation in nanostructured metals*, *Science*, 2006, vol. 312, no. 5771, pp. 249–251.
- [13] N. Kamikawa, X. Huang, N. Tsuji, N. Hansen, *Strengthening mechanisms in nanostructured high-purity aluminium deformed to high strain and annealed*, *Acta Mater.*, 2009, Vol. 57, no. 14, pp. 4198–4208.
- [14] E. Ma, T.D. Shen, X.L. Wu, *Less is more*, *Nat. Mater.*, 2006, vol. 5, no. 7, pp. 515–516.
- [15] W. Zeng, Y. Shen, N. Zhang, X. Huang, J. Wang, G. Tang, A. Shan, *Rapid hardening induced by electric pulse annealing in nanostructured pure aluminum*, *Scr. Mater.* 2012, vol. 66, no. 3–4, pp. 147–150.
- [16] Y. Miyajima, S. Komatsu, M. Mitsuhara, S. Hata, H. Nakashima, N. Tsuji, *Microstructural change due to isochronal annealing in severely plastic-deformed commercial purity aluminium*, *Philos. Mag.*, 2015, vol. 95, no. 11, pp. 1139–1149.
- [17] D. Terada, H. Houda, N. Tsuji, *Effect of strain on “hardening by annealing and softening by deformation” phenomena in ultra-fine grained aluminum*, *J. Mater. Sci.*, 2008, vol. 43, pp. 7331–7337.
- [18] A.M. Mavlyutov, T.A. Latynina, M.Yu. Murashkin, R.Z. Valiev, T.S. Orlova, *Effect of annealing on the microstructure and mechanical properties of ultrafine-grained commercially pure Al*, *Phys. Solid State*, 2017, vol. 59, no. 10, pp. 1970–1977.
- [19] T.S. Orlova, N.V. Skiba, A.M. Mavlyutov, M.Yu. Murashkin, R.Z. Valiev, M.Yu. Gutkin, *Hardening by annealing and implementation of high ductility of ultrafine grained aluminum: experiment and theory*, *Rev. Adv. Mater. Sci.*, 2018, vol. 57, no. 2, pp. 224–240.
- [20] T.S. Orlova, D.I. Sadykov, D.A. Kirilenko, A.I. Lihahev, A.A. Levin, *The key role of grain boundary state in deformation-induced softening effect in Al processed by high pressure torsion*, *Mater. Sci. Eng. A*, 2023, vol. 875, art. no. 145122.
- [21] T.A. Latynina, A.M. Mavlyutov, M.Yu. Murashkin, R.Z. Valiev, T.S. Orlova, *The effect of hardening by annealing in ultrafine-grained Al–0.4Zr alloy: influence of Zr microadditives*, *Philos. Mag. A*, 2019, vol. 99, no. 19, pp. 2424–2443.
- [22] T.S. Orlova, T.A. Latynina, A.M. Mavlyutov, M.Yu. Murashkin, R.Z. Valiev, *Effect of annealing on microstructure, strength and electrical conductivity of the pre-aged and HPT-processed Al–0.4Zr alloy*, *J. Alloys Compd.*, 2019, vol. 784, pp. 41–48.
- [23] W. Lefebvre, N.V. Skiba, F. Chabanaï, M.Yu. Gutkin, L. Rigutti, M.Yu. Murashkin, T. S. Orlova, *Vacancy release upon heating of an ultrafine grain Al–Zr alloy: in-situ observations and theoretical modeling*, *J. Alloys Compd.*, 2021, vol. 862, art. no. 158455.
- [24] T.S. Orlova, A.M. Mavlyutov, M.Yu. Murashkin, N.A. Enikeev, A.D. Evstifeev, D. I. Sadykov, M.Yu. Gutkin, *Influence of decreased temperature of tensile testing on the annealing-induced hardening and deformation-induced softening effects in ultrafine-grained Al–0.4 Zr alloy*, *Materials*, 2022, vol. 15, no. 23, art. no. 8429.
- [25] A.M. Mavlyutov, T.S. Orlova, E.Kh. Yapparova, *The effect of annealing and additional deformation on the mechanical properties of ultrafine-grained Al–1.5Cu alloy*, *Tech. Phys. Letters*, 2020, vol. 46, no. 9, pp. 916–920.
- [26] T.S. Orlova, D.I. Sadykov, D.V. Danilov, N.A. Enikeev, M.Yu. Murashkin, *Ultrafine-grained Al–Cu–Zr alloy with high-strength and enhanced plasticity*, *Mater. Lett.*, 2021, vol. 303, art. no. 130490.
- [27] T.S. Orlova, D.I. Sadykov, D.V. Danilov, M.Yu. Murashkin, *Influence of decreased temperature on the plasticization effect in high-strength Al–Cu–Zr alloy*, *J. Alloy Compd.*, 2023, vol. 931, art. no. 167540.
- [28] T.S. Orlova, A.M. Mavlyutov, M.Yu. Gutkin, *Suppression of the annealing-induced hardening effect in ultrafine-grained Al at low temperatures*, *Mater. Sci. Eng. A*, 2021, vol. 802, art. no. 140588.
- [29] M.Yu. Gutkin, T.A. Latynina, T.S. Orlova, N.V. Skiba, *Mechanism of hardening of ultrafine-grained aluminum after annealing*, *Phys. Solid State*, 2019, vol. 61, no. 10, pp. 1790–1799.
- [30] N.V. Skiba, T.S. Orlova, M.Yu. Gutkin, *Mechanism of implementation of high ductility in ultrafine-grained aluminum after annealing and subsequent deformation*, *Phys. Solid State*, 2020, vol. 62, no. 11, pp. 2094–2100.
- [31] M.Yu. Gutkin, T.S. Orlova, N.V. Skiba, *Micromechanism of the plasticity increase in ultrafine-grained Al–Cu–Zr alloy after annealing and additional deformation*, *Fiz. Tverd. Tela*, 2023, vol. 65, no. 5, pp. 875–879 (in Russian).
- [32] J. Gubicza, *Annealing-induced hardening in ultrafine-grained and nanocrystalline materials*, *Adv. Eng. Mater.*, 2020, vol. 22, no. 1, art. no. 1900507.
- [33] O. Renk, R. Pippan, *Anneal hardening in single phase nanostructured metals*, *Mater. Trans.*, 2023, vol. 64, no. 7, pp. 1464–1473.
- [34] M. Kato, *Thermally activated dislocation depinning at a grain boundary in nanocrystalline and ultrafine-grained materials*, *Mater. Sci. Eng. A*, 2009, vol. 516, no. 1–2, pp. 276–282.
- [35] M.A. Abdulstaar, E.A. El-Danaf, N.S. Waluyo, L. Wagner, *Severe plastic deformation of commercial purity aluminum by rotary swaging: Microstructure evolution and mechanical properties*, *Mater. Sci. Eng. A*, 2013, vol. 565, pp. 351–358.

- [36] M.M. Salem, E.A. El-Danaf, A.A. El-Enany, A.A. Radwan, *The mechanical properties and microstructure of aluminum alloy 1050 processed by ECAP in correlation to the imposed strain tensor*, J. Eng. Appl. Sci., 2008, vol. 55, pp. 125–144.
- [37] E.A. El-Danaf, M.S. Soliman, A.A. Almajid, M.M. El-Rayes, *Enhancement of mechanical properties and grain size refinement of commercial purity Al 1050 processed by ECAP*, Mater. Sci. Eng. A, 2007, vol. 458, no. 1–2, pp. 226–234.
- [38] T.S. Orlova, A.M. Mavlyutov, A.S. Bondarenko, I.A. Kasatkin, M.Yu. Murashkin, R.Z. Valiev, *Influence of grain boundary state on electrical resistivity of ultrafine grained aluminum*, Philos. Mag. A, 2016, vol. 96, no. 23, pp. 2429–2444.
- [39] T.S. Orlova, A.V. Ankudinov, A.M. Mavlyutov, N.N. Resnina, *Effect of grain boundaries on the electron work function of ultrafine grained aluminum*, Rev. Adv. Mater. Sci., 2018, vol. 57, no. 1, pp. 110–115.
- [40] R.Z. Valiev, F. Chmelik, F. Bordeaux, G. Kapelski, B. Baudalet, *The Hall-Petch relation in submicro-grained Al-1.5%Mg alloy*, Scr. Metall. Mater., 1992, vol. 27, no.7, pp. 855–860.
- [41] J.P. Hirth, J. Lothe, *Theory of Dislocations*, Wiley, New York, 1982.
- [42] V.V. Gertsman, A.A. Nazarov, A.E. Romanov, R.Z. Valiev, V.I. Vladimirov, *Disclination-structural unit model of grain boundaries*, Philos. Mag. A, 1989, vol. 59, no. 5, pp. 1113–1118.
- [43] X. Sauvage, N. Enikeev, R. Valiev, Y. Nasedkina, M. Murashkin, *Atomic-scale analysis of the segregation and precipitation mechanisms in a severely deformed Al-Mg alloy*, Acta Mater. 2014, vol. 72, pp.125–136.
- [44] X. Sauvage, A. Ganeev, Y. Ivanisenko, N. Enikeev, M. Murashkin, R. Valiev, *Grain boundary segregation in UFG alloys processed by severe plastic deformation*, Adv. Eng. Mater., 2012, vol. 14, no. 11, pp. 968–974.
- [45] Y. Liu, M. Liu, X. Chen, Y. Cao, H.J. Roven, M. Murashkin, R.Z. Valiev, H. Zhou, *Effect of Mg on microstructure and mechanical properties of Al-Mg alloys produced by high pressure torsion*, Scr. Mater., 2019, vol. 159, pp. 137–144.
- [46] M.P. Liu, H.J. Roven, M.Yu. Murashkin, R.Z. Valiev, A. Kilmametov, Zh. Zhang, Y. Yu, *Structure and mechanical properties of nanostructured Al-Mg alloys processed by severe plastic deformation*, J. Mater. Sci., 2013, vol. 48, pp. 4681–4688.
- [47] O. Andreau, J. Gubicza, N.X. Zhang, Y. Huang, P. Jenei, T.G. Langdon, *Effect of short-term annealing on the microstructures and flow properties of an Al-1% Mg alloy processed by high-pressure torsion*, Mater. Sci. Eng. A, 2014, vol. 615, pp. 231–239.
- [48] N.Q. Chinh, T. Csanádi, T. Györi, R.Z. Valiev, B.B. Straumal, M. Kawasaki, T.G. Langdon, *Strain rate sensitivity studies in an ultrafine-grained Al-30 wt.% Zn alloy using micro- and nanoindentation*, Mater. Sci. Eng. A, 2012, vol. 543, pp. 117–120.
- [49] K.V. Ivanov, E.V. Naydenkin, *Tensile behavior and deformation mechanisms of ultrafine-grained aluminum processed using equal-channel angular pressing*, Mater. Sci. Eng. A, 2014, vol. 606, pp. 313–321.
- [50] P. Kumar, M. Kawasaki, T.G. Langdon, *Review: Overcoming the paradox of strength and ductility in ultrafine-grained materials at low temperatures*, J. Mater. Sci. 2016, vol. 51, no. 1, pp. 7–18.
- [51] M.Yu. Gutkin, T.A. Latynina, T.S. Orlova, N.V. Skiba, *Mechanism of hardening of ultrafine-grained aluminum after annealing*, Phys. Solid State, 2019, vol. 61, no. 10, pp. 1790–1799.
- [52] N.V. Skiba, T.S. Orlova, M.Yu. Gutkin, *Mechanism of implementation of high ductility in ultrafine-grained aluminum after annealing and subsequent deformation*, Phys. Solid State, 2020, vol. 62, no. 11, pp. 2094–2100.
- [53] M.Yu. Gutkin, I.A. Ovid'ko, N.V. Skiba, *Crossover from grain boundary sliding to rotational deformation in nanocrystalline materials*, Acta Mater., 2003, vol. 51, no. 14, pp. 4059–4071.
- [54] M.Yu. Gutkin, I.A. Ovid'ko, N.V. Skiba, *Strengthening and softening mechanisms in nanocrystalline materials under superplastic deformation*, Acta Mater., 2004, vol. 52, no. 6, pp.1711–1720.
- [55] M.Yu. Gutkin, I.A. Ovid'ko, N.V. Skiba, *Emission of partial dislocations from triple junctions of grain boundaries in nanocrystalline materials*, J. Phys. D: Appl. Phys., 2005, vol. 38, no. 21, pp. 3921–3925.
- [56] M.Yu. Gutkin, I.A. Ovid'ko, N.V. Skiba, *Generation of deformation twins in nanocrystalline metals: theoretical model*, Phys. Rev. B, 2006, vol. 74, no. 17, art. no. 172107.
- [57] M.Yu. Gutkin, I.A. Ovid'ko, N.V. Skiba, *Crack-stimulated generation of deformation twins in nanocrystalline metals and ceramics*, Philos. Mag., 2008, vol. 88, no. 8, pp. 1137–1151.
- [58] I.A. Ovid'ko, N.V. Skiba, *Generation of nanoscale deformation twins at locally distorted grain boundaries in nanomaterials*, Int. J. Plast., 2014, vol. 62, pp. 50–71.
- [59] I.A. Ovid'ko, N.V. Skiba, *Nanotwins induced by grain boundary deformation processes in nanomaterials*, Scr. Mater., 2014, vol. 71, pp. 33–36.
- [60] I.A. Ovid'ko, N.V. Skiba, *Generation of nanoscale deformation twins at free surfaces in nanocrystalline and ultrafine-grained bulk materials, thin films and micropillars*, Rev. Adv. Mater. Sci., 2015, vol. 43, no. 1/2, pp. 22–30.
- [61] I.A. Ovid'ko, N.V. Skiba, *Formation of paired twins at grain boundaries in nanostructured and coarse-grained materials under plastic deformation*, Rev. Adv. Mater. Sci., 2016, vol. 47, no. 1/2, pp. 66–73.
- [62] I.A. Ovid'ko, N.V. Skiba, *Crossover from dislocation slip to deformation twinning in nanostructured and coarse-grained metals*, Rev. Adv. Mater. Sci., 2017, vol. 50, no. 1/2, pp. 31–36.
- [63] C.J. Smithells, E.A. Brands, *Metals Reference Book*, Butterworths, London, 1976.
- [64] A.P. Sutton, R.W. Balluffi, *Interfaces in Crystalline Materials*, Clarendon, Oxford, 1995.
- [65] S.W. Chan, V.S. Boyko, *Mobility of grain boundary dislocations during the conservative untwisting of [001] twist boundaries*, Phys. Rev. B, 1996, vol. 53, no. 24, pp. 16579–16586.
- [66] J. Monk, B. Hyde, D. Farkas, *The role of partial grain boundary dislocations in grain boundary sliding and coupled grain boundary motion*, J. Mater. Sci., 2006, vol. 41, pp. 7741–7746.
- [67] Y. Nasedkina, X. Sauvage, E.V. Bobruk, M.Yu. Murashkin, R.Z. Valiev, N.A. Enikeev, *Mechanisms of precipitation induced by large strains in the Al-Cu system*, J. Alloys Compd., 2017, vol. 710, pp. 736–747.

- [68] V.D. Sitdikov, M.Yu. Murashkin, R.Z. Valiev, *Full-scale use of X-ray scattering techniques to characterize aged Al-2wt.%Cu alloy*, J. Alloys Compd., 2018, vol. 735, pp. 1792–1798.
- [69] W. Xu, X.C. Liu, K. Lu, *Strain-induced microstructure refinement in pure Al below 100 nm in size*, Acta Mater., 2018, vol. 152, pp. 138–147.
- [70] M.Yu. Gutkin, N.V. Skiba, T.S. Orlova, *Grain-boundary nanoprecipitates-mediated mechanism of strengthening in Al-Cu-Zr alloy structured by high-pressure torsion*, Mater. Phys. Mech., 2022, vol. 50, no. 3, pp. 431–438.
- [71] V. Borovikov, M.I. Mendeleev, A.H. King, *Solute effects on interfacial dislocation emission in nanomaterials: Nucleation site competition and neutralization*, Scr. Mater., 2018, vol. 154, pp. 12–15.
- [72] S. Peng, Y. Wei, H. Gao, *Nanoscale precipitates as sustainable dislocation sources for enhanced ductility and high strength*, Proc. Natl. Acad. Sci. USA, 2020, vol. 117, no. 10, pp. 5204–5209.
- [73] J.M. Howe, W.E. Benson, A. Garg, Y.C. Chang, *In situ hot-stage high-resolution transmission electron microscopy of interface dynamics during growth and dissolution of  $\{111\}\alpha$ -Al<sub>2</sub>Cu plates in an Al-Cu-Mg-Ag alloy*, Mater. Sci. Forum, 1995, vol. 189–190, pp. 255–260.
- [74] S.J. Wang, G. Liu, J. Wang, A. Misra, *Characteristic orientation relationships in nanoscale Al-Al<sub>2</sub>Cu eutectic*, Mater. Charact., 2018, vol. 142, pp. 170–178.
- [75] G. Liu, M. Gong, D. Xie, J. Wang, *Structures and mechanical properties of Al-Al<sub>2</sub>Cu interfaces*, JOM, 2019, vol. 71, no. 4, pp. 1200–1208.
- [76] Q. Zhou, D.P. Hua, Y. Du, Y. Ren, W.W. Kuang, Q.S. Xia, V. Bhardwaj, *Atomistic study of atomic structures and dislocation nucleation at Al/Al<sub>2</sub>Cu interfaces*, Int. J. Plast., 2019, vol. 120, pp. 115–126.
- [77] G. Liu, S. Wang, A. Misra, J. Wang, *Interface-mediated plasticity of nanoscale Al-Al<sub>2</sub>Cu eutectics*, Acta Mater., 2020, vol. 186, pp. 443–453.
- [78] K.N. Mikaelyan, M.Yu. Gutkin, E.N. Borodin, A.E. Romanov, *Dislocation emission from the edge of a misfitting nanowire embedded in a free-standing nanolayer*, Int. J. Sol. Struct., 2019, vol. 161, pp. 127–135.
- [79] A.M. Smirnov, S.A. Krasnitskii, M.Yu. Gutkin, *Generation of misfit dislocations in a core-shell nanowire near the edge of prismatic core*, Acta Mater., 2020, vol. 186, pp. 494–510.
- [80] V.I. Vladimirov, M.Yu. Gutkin, S.P. Nikanorov, A.E. Romanov, *Defects of lamellar structure in unidirectionally solidified eutectic composites*, Mekh. Kompoz. Mater. (USSR), 1986, no. 4, pp. 730–733 (in Russian).
- [81] K.L. Malyshev, M.Yu. Gutkin, A.E. Romanov, A.A. Sitenikova, L.M. Sorokin, *Stress field and diffraction contrast of rod-shaped defects in silicon*, Sov. Phys.-Solid State (USA), 1988, vol. 30, no. 7, pp. 1176–1179.

УДК 538.91+539.52

## Эффекты упрочнения отжигом и разупрочнения при дополнительной пластической деформации в ультрамелкозернистых алюминии и сплавах на его основе: краткий обзор

Т.С. Орлова<sup>1,2</sup>, М.Ю. Гуткин<sup>2,3</sup>

<sup>1</sup> Физико-технический институт им. А.Ф. Иоффе Российской академии наук, Политехническая ул., 26, Санкт-Петербург, 194021, Россия

<sup>2</sup> Институт перспективных систем передачи данных, Университет ИТМО, Кронверкский пр., д. 49, лит А, Санкт-Петербург, 197101, Россия

<sup>3</sup> Институт проблем машиноведения Российской академии наук, Большой пр., В.О., д. 61, Санкт-Петербург, 199178, Россия

**Аннотация.** Дан краткий обзор последних экспериментальных и теоретических результатов о влиянии низкотемпературного отжига и последующей малой пластической деформации на микроструктуру, прочность и пластичность ультрамелкозернистого алюминия и сплавов на его основе, структурированных кручением под высоким давлением. Также кратко представлены некоторые более ранние результаты по этой проблеме для ультрамелкозернистого алюминия и сплавов на его основе, структурированных различными методами интенсивной пластической деформации. Подробно рассмотрены причины эффектов упрочнения отжигом и разупрочнения при дополнительной малой пластической деформации этих материалов. Кроме того, описано влияние температуры механических испытаний и легирующих элементов на эти эффекты. Показано, что физической основой этих эффектов являются трансформации дефектной структуры границ зерен в процессе низкотемпературного отжига и последующей малой пластической деформации ультрамелкозернистого алюминия и сплавов на его основе, структурированных кручением под высоким давлением.

**Ключевые слова:** ультрамелкозернистые материалы; Al; алюминиевые сплавы; неравновесные границы зерен; дислокации